Article

Evaluation of Bias-Corrected GCM CMIP6 Simulation of Sea Surface Temperature over the Gulf of Guinea

Oye Ideki * and **Anthony R. Lupo**

Atmospheric Sciences Program, School of Natural Resources, University of Missouri Columbia,
University Avenue, Columbia, MO 65211, USA; lupoa@missouri.edu
***** Correspondence: idekio@missouri.edu or oyelistic@yahoo.com

Abstract: This study used an ERA5 reanalysis SST dataset re-gridded to a common grid with a $0.25° \times 0.25°$ spatial resolution (latitude $\times$ longitude) for the historical (1940–2014) and projected (2015–2100) periods. The SST simulation under the SSP5-8.5 scenario was carried out with outputs from eight General Circulation Models (GCMs). The bias-corrected dataset was developed using Empirical Quantile Mapping (EQM) for the historical (1940–2015) and future (2030–2100) periods while the CMIP6 model simulation was evaluated against the ERA5 monthly observed reanalysis data for temperatures over the Gulf of Guinea. Overall, the CMIP6 models' future simulations in 2030–20100 based on the SSP5-8.5 scenario indicate that SSTs are projected, for the Gulf of Guinea, to increase by 4.61 °C, from 31 °C in the coast in 2030 to 35 °C in 2100, and 2.6 °C in the Western GOG (Sahel). The Linux-based Ncview, Ferret, and the CDO (Climate Data Operator) software packages were used to perform further data re-gridding and assess statistical functions concerning the data. In addition, ArcGIS was used to develop output maps for visualizing the spatial trends of the historical and future outputs of the GCM. The correlation coefficient (r) was used to evaluate the performance of the CMIP6 models, and the analysis showed ACCESS 0.1, CAMS CSM 0.2, CAN ESM 0.3, CMCC 0.3, and MCM 0.4, indicating that all models performed well in capturing the climatological patterns of the SSTs. The CMIP6 bias-corrected model simulations showed that increased SST warming over the GOG will be higher in the far period than the near-term climate scenario. This study affirms that the CMIP6 projections can be used for multiple assessments related to climate and hydrological impact studies and for the development of mitigation measures under a warming climate.

Keywords: sea surface temperature projection; CMIP6; bias correction; general circulation model; Gulf of Guinea; Western Sahel; ocean warming

1. Introduction

The critical role of the ocean in the Earth's climate system is well known and documented, as the ocean is the largest carbon sink and heat reservoir absorbing over 93% of heat generated since the Industrial Revolution [1]. However, evidence in the scientific literature affirms that the last few decades have witnessed a significant increase in the heat storage capacity of the ocean with a deleterious impact on key components of the Earth–atmosphere system [2]). The observed ocean-warming manifestation includes an increase in the average sea surface temperature and changes in ocean circulation, stratification, heat transport, ocean biogeochemistry, and marine heat waves with concomitant effects on regional and global climate variabilities and human societies [3]. It is on record that the average global sea surface temperature (SST) of the ocean has had a significant warming trend of ~0.13 °C per decade since the beginning of the 20th century, with the SSTs of the last three decades considered the warmest since the commencement of modern instrumental records [4] with global warming implicated in the observed warming effect.

Several studies have been conducted over the years to examine global sea surface temperature distributions and their influence on climate extremes over the West African

region. The above assertion hinges on the fact that the amount of near-surface moisture for convective rainfall is sensitive to sea surface temperature anomalies through the Clausius–Clapeyron relationship [5]. Another mechanism where SST influence is evident is in the tropical Atlantic Ocean through the interaction with the wind field, in which the weakness of the trade winds over the Equator forces the Intertropical Convergence Zone to migrate northwards, thereby strengthening southerly trade winds. This interaction ultimately leads to upwelling, vertical missing, and evaporation into the atmosphere, and eventually leads to a phenomenon called cold tongue, which develops in May, June, and July, persisting till September. It is this seasonal SST anomaly that exercises significant control over rainfall patterns in the West African climate [6].

Consequently, modeling studies by [7,8] corroborate the above analogy on the influence of ocean forcing on rainfall variability in Sub-Saharan Africa. Similar studies have also focused on the impacts of localized SST anomalies over the coast of Guinea and the eastern Atlantic Ocean [9]. Ref. [10] studies in 1987 were more emphatic as they revealed that the reduction in rainfall in the Sahel during winter corresponded well with the warm SST anomaly of the Guinea coast; the global sea surface temperature (SST) variability merely slightly moderated its effects.

Ref. [11] in his study assessed the impacts of warming/cooling of the Atlantic Sea surface temperature (SST) on the climate in West Africa using Version 4.4 of the Regional Climate Model (RegCM4.4A.) The study outcome revealed that the 1–2 K cooling and warming of the Atlantic SST will result in triple temperature and precipitation change structures over West Africa as well as an anomalous dipole of precipitation, resulting in opposite signs over the Sahel and the Gulf of Guinea.

Given the scale and vulnerability of West Africa, described as one of the most populated regions of the world, to extreme climate events, climate change is manifested in an increased frequency of floods and droughts, with devastating impacts on people's livelihoods and the attainment of sustainable development goals [12]. The vulnerability is further driven by a range of factors that include a weak adaptive capacity, dependence on productive resources that are climate-sensitive, Africa's geographical location in the lower latitudes, and widespread poverty climate change, which is also disrupting the hydrological cycle, putting a strain on water resources, population displacement, and food insecurity [13]. This has led the scientific community to recognize the need to mobilize additional resources to mitigate the projected impact of climate change on critical sectors of the economy in the sub-region and to build resilience. This is against the backdrop that a warmer climate holds more moisture, implying an increased frequency of rainfall events. Conversely, rising temperatures accelerate evaporation and can intensify drought episodes [14].

The Fourth Assessment Report of the Intergovernmental Panel on Climate Change (IPCC) (AR4) projected a warming rate of 0.5–2.5 K over the Atlantic Ocean for the twenty-first century [15] based on all the Special Reports on Emissions Scenarios (SRESs), while the Fifth Assessment Report of the IPCC also projected a temperature change of 0.2–2.3 K over West Africa [16] based on all the Representative Concentration Pathways (RCPs). In the same vein, the Sixth Assessment Report (AR6) of the IPCC 2022 affirms that the global mean SST has increased since the beginning of the 20th century by 0.88 °C, with significant warming projected in the coming decades.

The increase in the SST is reported to be driven by climate change at an oceanic scale, such as the Atlantic Equatorial Mode and El Niño Southern Oscillation (ENSO) [17,18]. Thus, the understanding of future climate change effects on SST variability and warming in the Gulf of Guinea has become pertinent to investigate. The General Circulation Model (GCM) outputs of the Coupled Model Intercomparison Project (CMIP) are an essential dataset for forecasting future climate trends. The main difference between the previous CMIP5 models and the current CMIP6 output is based on the set of future scenarios used to project climate evolution. The CMIP6 model was designed to bridge and improve the restrictions identified in the CMIP5 models with a focus on identifying systematic errors in simulations and improving the representation of land use changes in the climate (IPCC

report 2013). Several new scenarios are used by CMIP6 called Shared Socioeconomic Pathways (SSPs), which are combined with previous CMIP5 scenarios of climate radiative forcing called Radiative Concentration Pathways (RCPs). The GCMs of Coupled Model Intercomparison Project 6 (CMIP6) are the most advanced tools currently available for climate studies and are better than previous projects. Moreover, the GCMs of Coupled Model Intercomparison Project 6 (CMIP6) are also the most advanced tools currently available for climate studies and for simulating past and future extreme climate events, given the scale of anthropogenic-induced global warming [19–21].

However, GCM simulations cannot be directly used for climate impact studies because of their inability to give reliable information at a local scale [22]. Furthermore, GCM outputs are often coarse in their temporal and spatial dimensions, resulting in systematic biases [23]. Hence, it is critical to validate the abilities of these models before use for any climate projection and impact studies. Therefore, downscaling model outputs is necessary to improve the model resolution to match the resolution at a local scale. Downscaling is essentially the process where spatial data are represented by lower spacing and smaller temporal intervals [24].

Bias correction is a technique employed for resolving high-resolution Global Circulation Model (GCM) and Regional Climate Model (RCM) outputs known to exhibit systematic biases [25]. This is important, given the fact that General Circulation Models (GCMs) provide valuable information dealing with historical and future larger-scale climate trends; unfortunately, as pointed out above, their resolution is too coarse to investigate the localized impact effects of extreme climate events [26,27]. Furthermore, as stated by [27], raw GCM outputs are characterized by a non-trivial degree of bias and the seeming limitation that often affects the ability of GCMs to reproduce extreme tails of climate variables [28]. It has therefore become imperative that, before GCM/RCM outputs are applied for use in hydrological [29,30], agricultural, and climate risk assessments, they must be downscaled to a finer resolution and bias-corrected as far as the observed data are concerned [31,32]. Hence, bias correction can be described as a post-processing technique in climate data to achieve a more realistic and consistent representation of atmospheric processes at very high and fine spatial scales.

The evidence in the literature affirms that statistical and dynamic approaches are the most common methods used for the downscaling and bias correction of projections involving climate variables from GCMs. The statistical approach is based on the distribution and relationship between the observed and projected data for the historical period [29,33]. Secondly, in statistical downscaling, statistical relationships between coarse-scale climate variables and locally observed data are established, including integrating the effects of fine-scale predictors into downscaled data [34]. The dynamical approach, on the other hand, is based on a regional climate model forced with the boundary conditions from coarse-resolution GCMs [35,36].

The process of downscaling also requires the conversion of the model output from a course to a finer resolution, especially when a Regional Climate Model (RCM) is forced with a GCM, resulting in finer-scale output where regional climate processes, topography, and orography are incorporated [37]. Despite the advantages of dynamical downscaling, its limitation stems from the fact that it is computationally intensive and can introduce additional biases [38,39]. Statistical downscaling has been extensively deployed in many studies due to its efficiency and can be applied to a variety of climate variables in topographically challenged terrain [36,40].

However, downscaling is complemented by bias correction, a procedure in which the climate model output is adjusted such that its statistical properties (e.g., mean, variance, and potentially higher moments) resemble those of observations in a common climatological period [27,41]. This study adopts the nonparametric statistical transformation-based bias correction, which shows better skills in comparison to the parametric method in reducing biases from GCM outputs [42]. The success and applicability of bias correction for the

projection of future climate variables were proven by several studies conducted by [30,43–45], indicating the performance and acceptability of the bias correction method.

Dynamical downscaling and statistical downscaling have emerged as some of the best methods widely used for post-processing. The statistical approach has advantages over dynamical downscaling as it is a lot less resource intensive [33], Additionally, the pros and cons of both approaches are that, while statistical approaches are based on the distribution and relationship between the observed and projected data for the historical period, dynamical downscaling, on the other hand, is based on a regional climate model forced with the boundary conditions from the coarse-resolution global circulation model [46]. Given the gap identified in the literature on the use of GCM CMIP6 models for simulating the historical and future SSTs of the Gulf of Guinea, it has become critical to examine the skills of CMIP6 models in simulating the sea surface temperature over the Gulf of Guinea.

The importance of the analyses of the historical and predicted future sea surface temperatures (SSTs) of the Gulf of Guinea cannot be overemphasized as they provide a framework to better understand and assess the predictability of extreme climate events and their impacts under a warming climate scenario.

The motivation for this research originates basically from the need to accurately understand and address future climate impacts in Africa both at the regional and local scales and the imperative for climate data products to represent climate extremes accurately and be available at fine and temporal resolutions [47]. This requires the deployment of bias correction techniques to rectify the problem associated with GCM simulations to generate reliable information at a local scale, which can be used for the formulation of climate adaptation strategies in Africa in the face of the increased frequency and severity of climate extremes.

The objectives of this study therefore are to evaluate the performance of 8 GCM-CMIP6 models in simulating the historical sea surface temperatures of the Gulf of Guinea in 1970–2014. Secondly, we used bias-corrected CMIP6 outputs to simulate future SST projections (2015–2100) and finally used statistical techniques to quantitatively validate the performance of the models.

2. Materials and Methods

Projections from the General Circulation Models (GCMs) play a vital role in understanding future climate changes. However, the spatial resolution at which GCMs are run is often too coarse to obtain reliable projections at the regional and local scales [48]. In addition, the Linux-based Ncview, Ferret, and Climate Data Operator (CDO) software packages were used to perform further data re-gridding and statistical functions on the data, while ArcGIS was used to develop output maps for visualizing the spatial trends of the historical and future outputs of the GCMs.

The bias-corrected dataset was developed using Empirical Quantile Mapping (EQM) for the historic (1940–2014) and projected (2015–2100) climates for the SSP5-8.5 scenarios using outputs from 8 General Circulation Models (GCMs) from Coupled Model Intercomparison Project-6 (CMIP6). Empirical Quantile Mapping (EQM) is one of the most common tools used for correcting the biases of climate model simulations, where it maps between simulated and observed Cumulative Distribution Functions (CDFs) that are empirically constructed based on the data from a historical period [49]. One of the advantages of Empirical Quantile Mapping (EQM) is that it is very simple and robust to use and thus provides a better performance for the bias correction of stationary data. The EQM assumes that the distribution of the simulated or estimated data preserves the distribution of any observed data. In Empirical Quantile Mapping (EQM), simulated data corresponding to a given probability are replaced by an observed quantile corresponding to the same probability. In addition, EQM has become attractive as a bias correction method given its ability to correct the mean, standard deviation, and higher-order distributional moment [50].

Empirical Quantile Mapping (EQM) can also be used to correct the biases of GCM-RCM projections by replacing the empirical CDFs with a parametric distribution. Just like EQM, it was assumed that both the GCM-RCM simulated and observed precipitations

followed a specific frequency distribution. The gamma distribution is commonly used for representing the CDF of precipitation and the method is referred as to as Gamma Quantile Mapping (GQM). The quantile mapping technique removes the systematic bias from the GCM simulations and has the benefit of accounting for GCM biases in all statistical moments; though, like all statistical downscaling approaches, it is assumed that biases relative to historical observations will be constant in the projection period [32] Therefore, selecting an appropriate probability distribution model is imperative for successfully implementing the Empirical Quantile Mapping (EQM) method.

Furthermore, Empirical Quantile Mapping (EQM) corrects the distribution of simulated data to match the distribution of the observation dataset [51]. Quantile mapping also attempts to remove quantile-dependent biases. This is performed with the help of the Transfer Function (TF). The following highlights some of the other methods of bias corrections that are available in the literature.

2.1. Delta-Correction Method

The delta-change method of bias correction according to [52] provides climate scenarios by adding the future change signal (anomalies) from GCM-RCM simulations arising from changes in the observational datasets rather than using the GCM-RCM simulations of future conditions directly. This method was adjudged the simplest bias correction method to use and used observations as a basis. Therefore, it was stable and robust enough to produce future climate variable dynamics, like current conditions [53].

2.2. Adjusted Quantile Mapping Method

The adjusted quantile mapping method was used to calculate the variations of each quantile in the CDFs of daily simulated data between the control or historical periods and what would be simulated in the future. The changes established by each of the quantiles were reorganized based on the CDFs of the observed data for the same control period. The new CDFs were obtained to transmit the climate change signal by adding these observations to each quantile [54]. Detailed information on the application of the AQM method can be found in [55].

2.3. Gamma-Pareto Mapping Method

This method is a combination of the gamma distribution and a Generalized Pareto Distribution (GPD) in quantile mapping [56]. Gamma-Pareto mapping guarantees a better correction of higher percentiles. Although the method was developed for precipitation, the evidence in the literature affirms that it can be applied for Gaussian variables, like temperature, and is normally used in a study where a normal distribution is fitted for values between the 5th and 95th percentiles, while the upper and lower 5% values are assumed to follow the GPD.

The method has a good success rate and is often described as a better correction technique involving higher percentiles (extremes). The basic assumption of the method is that the lower 95% of the distribution follows the gamma distribution. The upper 5% are assumed to follow the general Pareto distribution. Several studies on climate change scenarios were used with outstanding success [57].

2.4. Quantile Delta Mapping

Quantile delta mapping as a method of bias correction was first proposed by [58], essentially to preserve the trends in climate simulations and to take some non-stationarity into account. Ref. [59] performed a comparison of QDM with other quantile mapping methods and found that QDM outperformed the other methods in the case of the preservation of trends. Another advantage of Quantile Mapping (QM) is that it can be deployed to correct the biases of GCM-RCM projections by replacing the empirical CDFs with a parametric distribution. QDM is similar to EQM as it holds the assumption that both the GCM-RCM simulated and observed precipitations follow a specific frequency distribution. The gamma

distribution is commonly used for representing the CDF of precipitation and the method is referred to as Gamma Quantile Mapping (GQM).

2.5. Moving Window Technique

This method normally operates where the entire data are used to calibrate the models. The moving window technique can also be applied to correct daily and monthly climatic variables and has extensively been used by [44,60]. The technique focuses on a moving window centered on each day of the year to calibrate a correction. Hence, there is a correction function for each day of the year, rather than a single correction function for the whole period. The moving window technique was not used in GPQM, as it did not have enough data to fit the generalized Pareto distribution for the extremes. Hence, this moving window was used for four bias correction methods, except for GPQ.

Having examined the strengths and weaknesses of the other methods mentioned above, this study adopted the empirical quantile mapping method. The bias-corrected dataset was then evaluated against the observations for monthly and annual sea surface temperatures (SSTs) over the Gulf of Guinea, as shown in Table 1.

**Table 1.** Brief description of the CMIP6 GCM models used in this study.

Data	Type	Temporal	Historical	Future
ERA5	Observed	Monthly	1940–2014	---
ACCESS-CM2 (Australia)	Model	Monthly	1940–2014	2030–2100
CAMS-CSM1-0 (China)	Model	Monthly	1940–2014	2030–2100
CanESM5-CanOE (Canada)	Model	Monthly	1940–2014	2030–2100
CMCC-ESM2 (Italy)	Model	Monthly	1940–2014	2030–2100
HadGEM3-GC31-LL (UK)	Model	Monthly	1940–2014	2030–2100
EC-Earth3-CC (Europe)	Model	Monthly	1940–2014	2030–2100
MCM-UA-1-0 (USA)	Model	Monthly	1940–2014	2030–2100
MPI-ESM1-2-LR (Germany)	Model	Monthly	1940–2014	2030–2100

The observed monthly gridded SST for the Gulf of Guinea for the 1940–2014 period was obtained from the ERA5 Copernicus data at a $0.25° \times 0.25°$ spatial resolution.

The mean monthly SSTs from 8 CMIP6-GCMs were obtained from https://esgf-node.llnl.gov/search/cmip6/, accessed on 1 July 2023. The SST variables were available for both the historical and future scenarios from the 8 CMIP6-GCMs used in this study. The spatial resolution of the CMIP6 projection varied from $0.7°$ (EC-Earth3) to more than $2°$ (MCM-UA-1-0 (USA)). It is important to emphasize that both the historical (1940–2014) and the future simulations (2015–2030) were based only on ssp585 scenarios under the *r1i1p1f1* initial condition at a monthly time scale basically due to the limited computing resources. The scenarios used in the CMIP6 combined Shared Socioeconomic Pathways (SSPs) and targeted radiative forcing levels at the end of the 21st century [61]. SSP585 is based on the emission scenario considering SSP-5 and the radiative forcing of 8.5 watts/m^2 at the end of the 21st century. It is also characterized by high challenges to mitigation and low challenges to adaptation [62].

2.6. The Study Area

The study area was the GOG region located southeast of the Atlantic Ocean. The area lies between the longitudes of $10°$ W and $8°$ E and latitudes of $5°$ N and $5°$ S, and, thus, south of West Africa, as shown in Figure 1. The hydrography of the GOG is directly affected by five main currents, namely, Benguela, the South Equatorial, the Canary, the Counter Equatorial, and the Guinea currents [63].
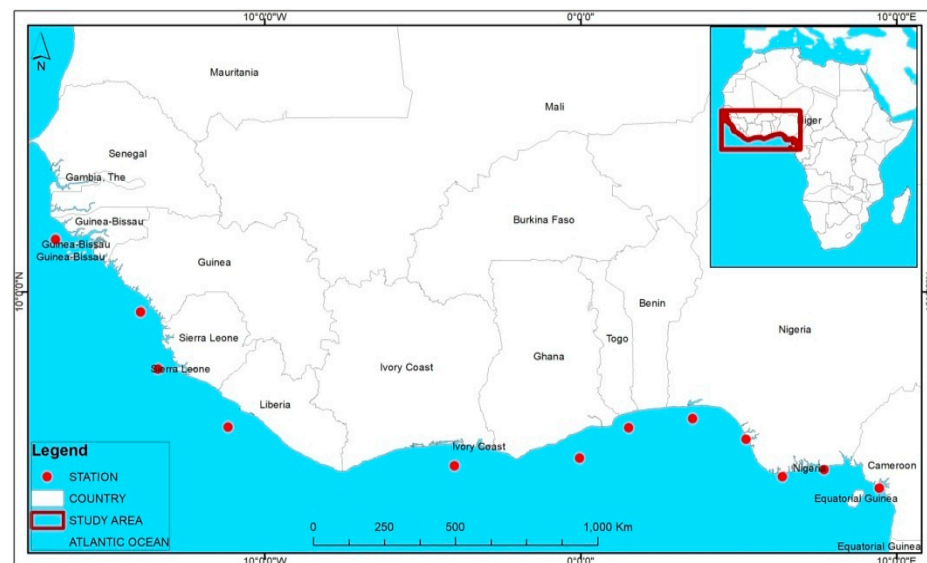
Figure 1. Map of the study area showing the Gulf of Guinea.

The tropical marine (mT) air mass and the tropical continental (cT) air mass are the two main wind currents that have the greatest impact on the climate of the GOG and West Africa. The Equatorial Easterlies, a third wind current, is only significant over the continent of West Africa [64,65]. The southern high-pressure band off the coast of Namibia is where the mT air mass starts. On its path, the air mass takes up moisture over the South Atlantic Ocean, crosses the Equator, and then penetrates the GOG and West Africa. The high-pressure area to the north of the Tropic of Cancer is where the cT air mass is found. It picks up little moisture along its path and is thus dry. The two air masses (mT and cT) meet along a slanting surface called the Inter-Tropical Discontinuity (ITD). The Equatorial Easterlies are rather erratic, cool air masses, which come from the east and flow in the upper atmosphere along the ITD.

3. Results

3.1. Historical/Observed SST Climatology

An attempt is made here to examine the patterns of observed SSTs (1940–2014) before proceeding to evaluate CMIP6 bias-corrected future projections (2030–2100). The individual model projection is discussed as follows:

The spatially averaged seasonal sea surface temperature cycle over the Gulf of Guinea, as shown in Figure 2, reveals that considerable biases exist between the corrected GCM-RCM outputs and observations, which ultimately necessitate against the direct application of GCM-RCM sea surface temperature projections to local climate change studies over the Guinean coast. The seasonal pattern of SST variability was also assessed in the study, and the result of the geospatial analysis, as shown in Figure 3, revealed a marked variability, with June–July and August (JJA) recording the lowest values (28.18 °C for the Guinean coast and 24.70 °C in the Western Sahel), followed by 28.71 °C for the Guinean coast in the fall months of December, January, and February (DJF) and 20.85 °C for the Western Sahel. Conversely, the spring months of March, April, and May (MAM) recorded the highest levels, given the variability values of 29.34 °C for the Guinean coast and 20.08 °C in the Sahel, while the variability values for the fall months of September, October, and November (SON) exhibited 28.74 °C for the Guinean coast and 25.62 °C for the low-rainfall region. Generally, the result of the seasonal pattern indicates that the SSTs for the Guinean coast are generally low in June, July, and August (JJA), followed by September, October, and November (SON), while March, April, and May (MAM) and December, January, and February are characterized by high SST values. The anomalously cold SSTs observed in June, July, and August (JJA), and September, October, and November along the Guinea

coast were attributed to the influence of the coastal upwelling of cold water from below the sharp, shallow thermocline. The upwelling of nutrients has been reported to impact marine ecosystems negatively [6,63].
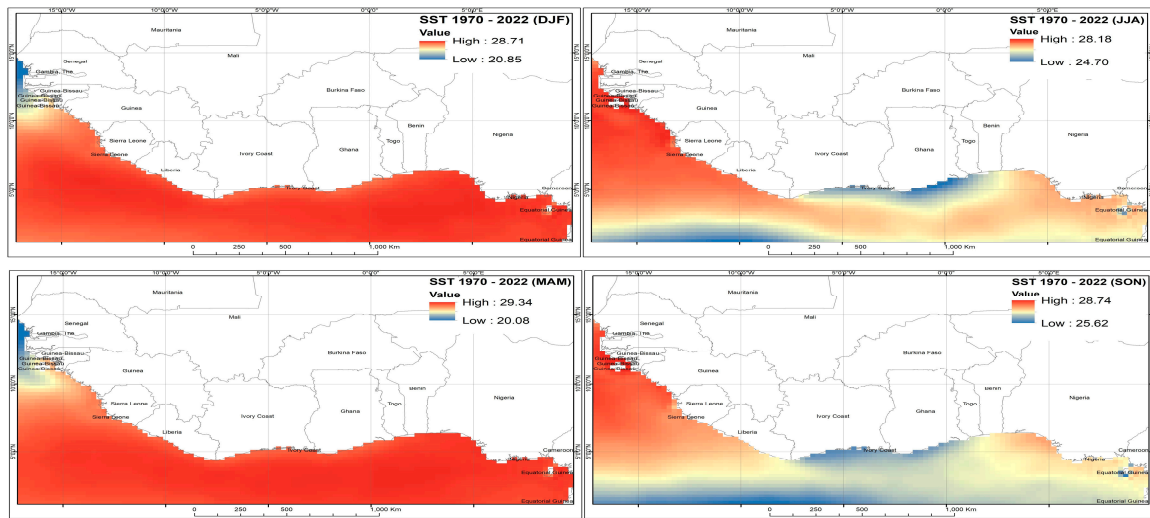

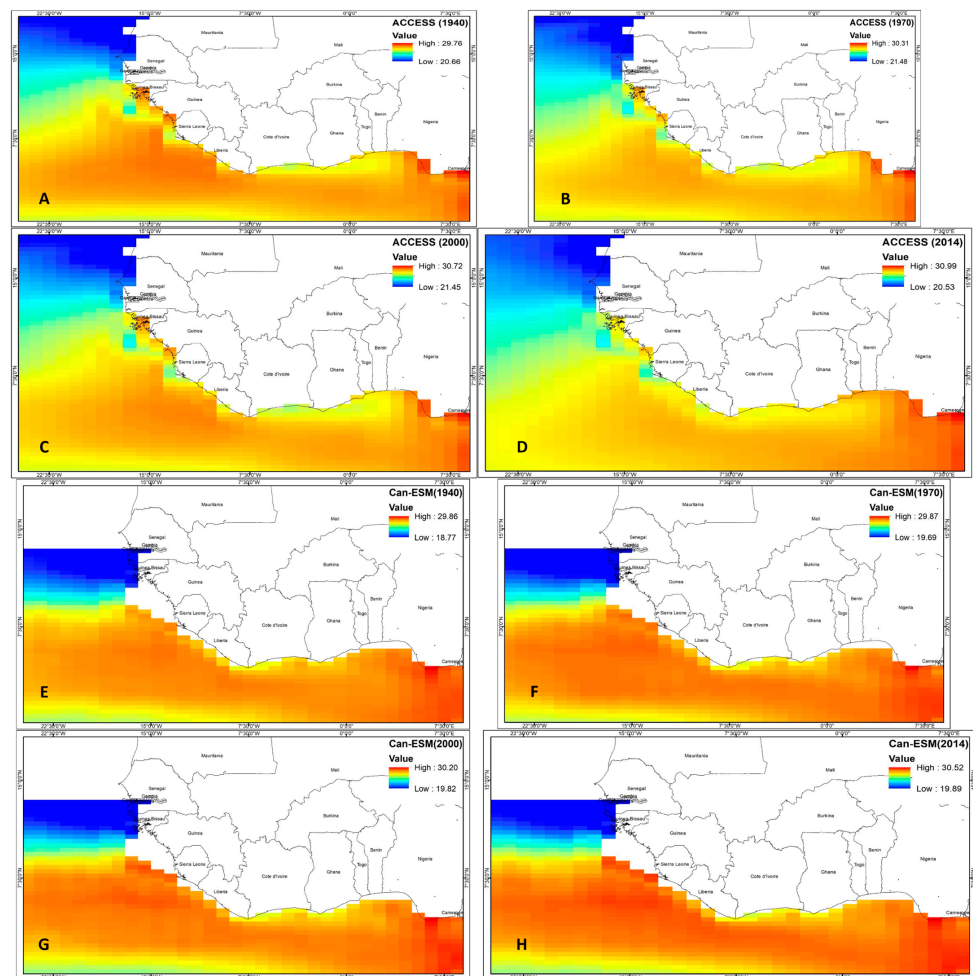**Figure 2.** Seasonal patterns of SST variability.

Figure 3. ACCESS historical model showing (**A**) 1940, (**B**) 1970, (**C**) 2000 and (**D**) Can-ESM CMIP6 models' historical outputs showing: (**E**) 1940, (**F**) 1970; (**G**) 2000; (**H**) 2014.

In comparison with the uncorrected observed seasonal SSTs discussed above and the result of the analysis carried out on the historical sea surface temperature by the bias-corrected GCM ACCESS-CM2 in 1940 for the Gulf of Guinea (GOG), as shown in Figure 3A–D a warm bias of 29.76 °C for the high-warming GOG and a cold tongue of 20.66 °C for the low-warming GOG can be observed. In 1970, the model captured 30.31 °C for the Guinean coast and 21.48 for the Western Sahel (low), while in 2000, 20.72 °C was simulated for the warming regions of the GOG and 21.45 °C for the Western Sahel. The observed sea surface temperature (SST) for 2014 for the Guinea coast was 30.96 °C and 20.53 °C for the Western Sahel.

The inter-annual change in the historical SST climatology as revealed by ACCESS-CM2 from 1940–2014 was 1.23 °C while that of the Western Sahel is 0.13 °C with most of the warming concentrated in 1970 and 2000 in the Western Sahel while the year 2014 was remarkable as it recorded the highest Sea surface temperature (30.99 °C) of the Guinean coast. A close examination of the uncorrected observed seasonal cycle of the Gulf of Guinea's sea surface temperature and the bias-corrected ACCESS model indicates the excellent performance of the models in being able to reproduce the historical sea surface temperatures for the study and key climate features of the study domain.

The Can-ESM model's historical sea surface temperature in 1940–2014 was 29.86 °C, denoted as high, for the Guinean coast and 18.77 °C for the Western Sahel, denoted as low, as shown in Figure 3E. In 1970, the model captured 29.87 °C as the sea surface temperature for the Guinea coast and 19.64 °C for the Western Sahel, as shown in Figure 3F, while the year 2000's historical sea surface temperature for the Guinea coast, represented in Figure 3G was 30.20 °C (high) and 19.82 °C (low). In 2014, the model captured 30.52 °C for the high-warming Guinea coast and 19.89 °C for the anomalously low-warming Western Sahelas captured in Figure 3H. On average, the SST increased by 0.66 °C in the GOG and 1.12 °C in the Western Sahel. The result of the Can-ESM model demonstrates that the study domain is characterized by progressive warming over the years.

CAMS-CSM1-0, shown in Figure 4A–D captured the mean SST climatology in 1940 as 29.11 °C for the high-warming GOG region and 18.56 °C for the low-warming region of Western Sahel, while in 1970, the SSTs were 29.80° and 19.26° for the high- and low-warming regions, respectively. In 2000, the historical SST mean values were shown as 29.84 °C and 19.87 °C for the low-warming region. In 2014, the high-warming region recorded 29.77 °C and 19.56 °C for the high and low values, respectively, indicating that the SST increased by 0.66° in 1940–2014 for the Guinean coast and 0.18 °C for the low region (Western Sahel). On average, the SST increased by 0.66 °C in the GOG and 1.12 °C in the Western Sahel.
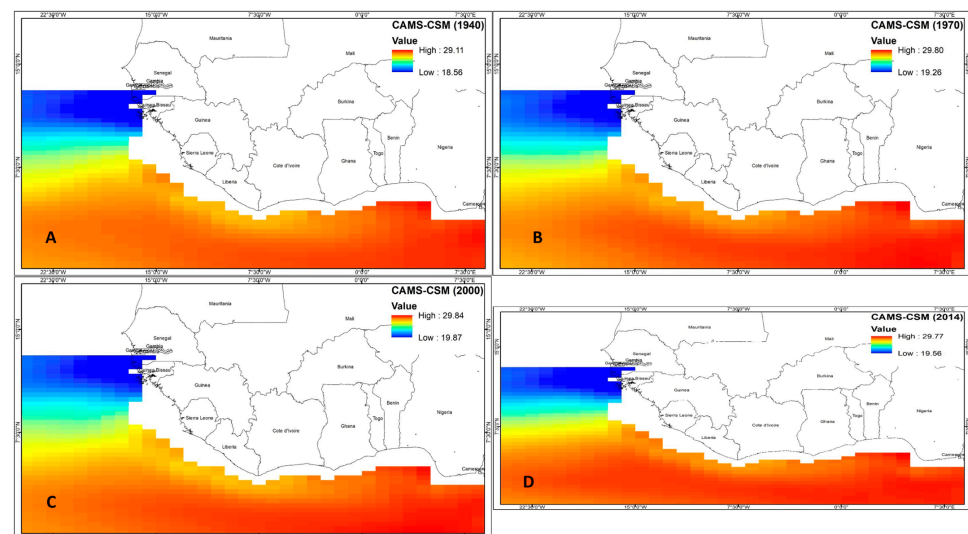

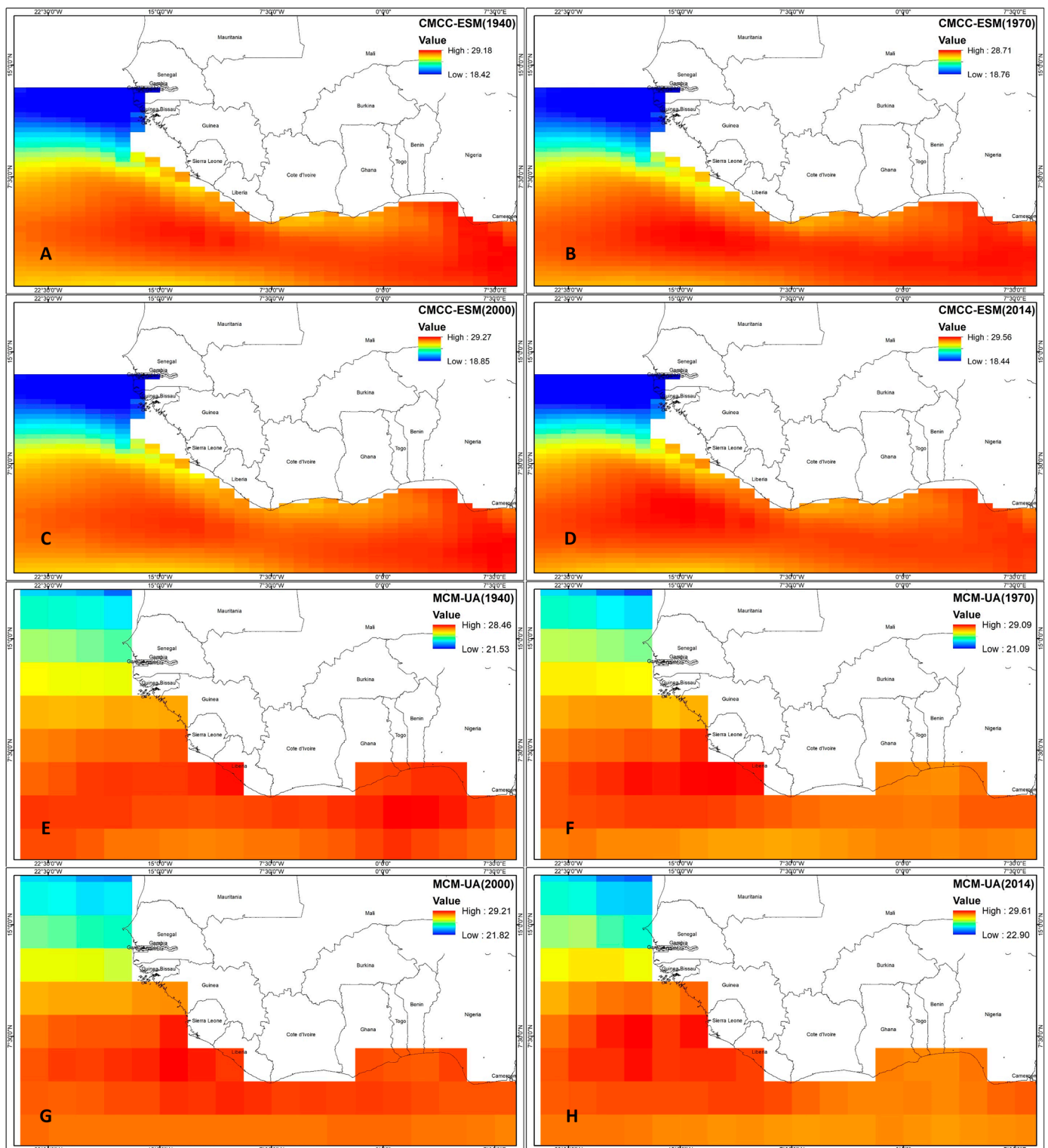**Figure 4.** CMIP6 CAMS-CSM model's historical simulation.

The CMCC-ESM model simulation of the historical SST of the GOG in 1940, shown in Figure 5A–D, was 29.18 °C (high), and 18.42 °C in the Western Sahel. The 1970 mean SST value for the high-warming region of the Guinean coast, however, contrasted with 28.71 °C and 18.76 °C for the low-warming region. The year 2000 saw an upward increase in the mean SST of the Gulf of Guinea, recording 29.27 °C and 18.46 °C for the high- and low-warming regions, respectively. The highest increase was in 2014 with 29.56 °C and 18.44 °C for the Guinean coast and Western Sahel, respectively, as presented in Figure 5D.
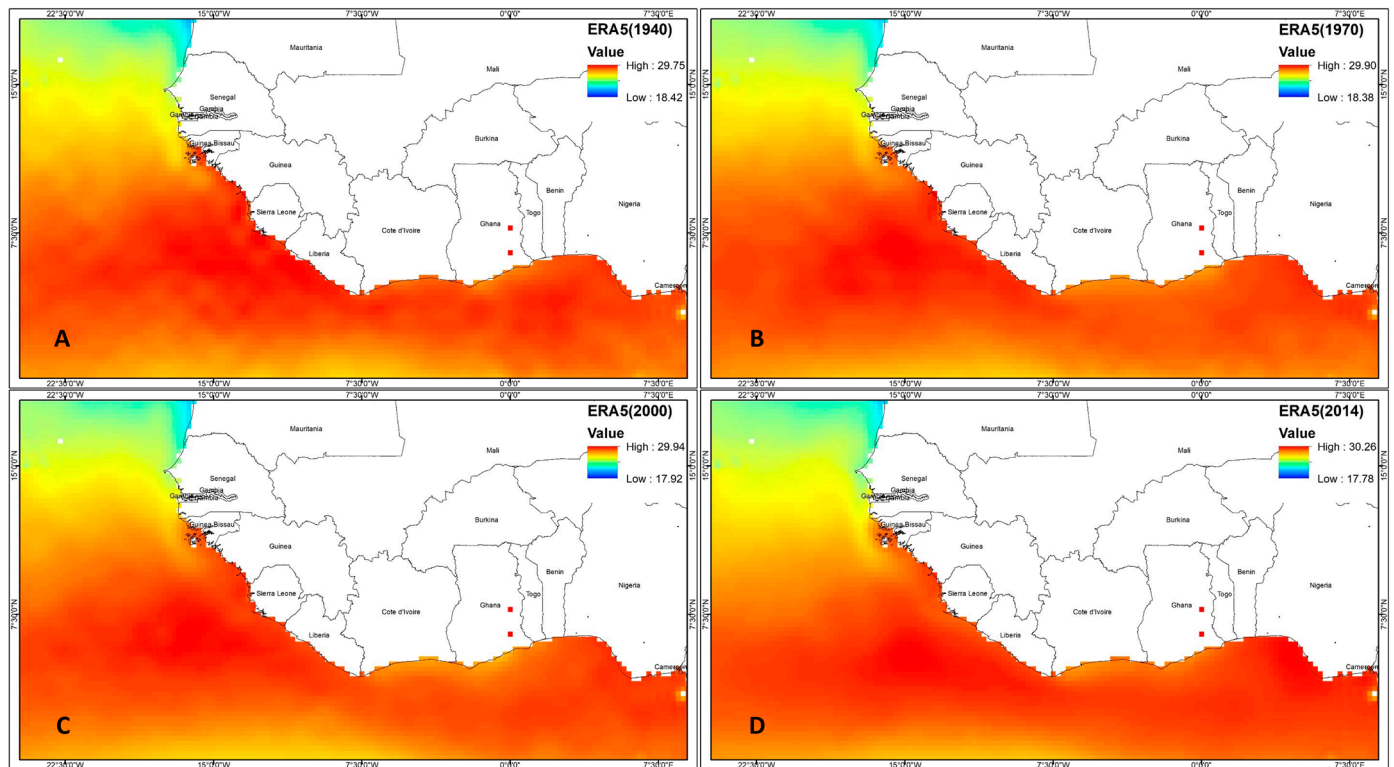
Figure 5. ERA 5 observed sea surface temperature dataset.

Similarly, ERA5, as shown in Figure 5A–D, which is the observed data, indicates that in 1940, the mean SST is 29.75 °C for the high-warming region and 18.42 °C for the Western Sahel, while in 1970, a significant increase in the mean SST is recorded at 29.80 °C for the Guinean coast and 18.38 °C for the low-warming region. Again, in 2000, as shown in Figure 4B, the Guinean coast is represented by the high values recorded as 29.94 °C and 17.92 °C for the low value. In 2014, the ERA5 historical data had a mean SST value of 30.25 °C for the Guinean coast and 17.78 °C for the Western Sahel, implying the SST increased by 0.55 °C during this period.

The MCM-UA model evaluation of the SST historical data, as shown in Figure 6A–H, indicates an annual SST mean value of 28.46 °C in 1940 for the high-warming region representing the Guinean coast and 21.53 °C for the low-warming area representing the Western Sahel, while an increasing trend can be observed in 1970 with 29.09 °C for the high- and 21.09 °C for the low-warming regions. In 2000, the increasing SST trend continued for the high-warming and low-warming regions with 29.21 °C and 21.82 °C, respectively. The pattern of observation was not different in 2014 as the individual model captured 29.61 °C as the highest value for the high-warming region of the GOG and 22.90 °C for the low.

Figure 6. CMIP6 CMCC historical simulation showing (**A**) 1940; (**B**) 1970; (**C**) 2000; (**D**) 2014. MCM-UA models' historical simulations showing (**E**) 1940; (**F**) 1970; (**G**) 2000; (**H**) 2014.

Given the outcome of the analysis above, it is evident that the SST increases by an average of 1.15 °C in 1940–2014 for the GOG and 1.37 °C for the low-warming region (Sahel). This further indicates that all the model ensembles are consistent in capturing the interannual variability of the mean SST climatology with some level of accuracy.

3.2. CMIP6's Future SST Projection

Bias-corrected CMIP6 climate models derived from GCM data using empirical quantile mapping for simulated future SST patterns are presented below based on RCP 8.5 for the Gulf of Guinea (GOG) and the Western Sahel. Having presented the SST historical patterns above, the decadal projections of the SSTs in 2030–2100 are hereby discussed as follows.

The ACCESS-CM2 model simulation of the future sea surface temperatures for 2030 for the high-warming region of the GOG, shown in Figure 7A, are projected to be 30.87 °C and 21.77 °C for the Western Sahel. In 2040 (Figure 7B), further significant warming is projected for the Guinean coast at 31.90 °C and 21.73 °C for the Western Sahel, while the future projection for 2050 puts the sea surface temperatures of the Guinea coast at 32.30 °C and 21.63 °C for the Western Sahel, as shown in Figure 7C.
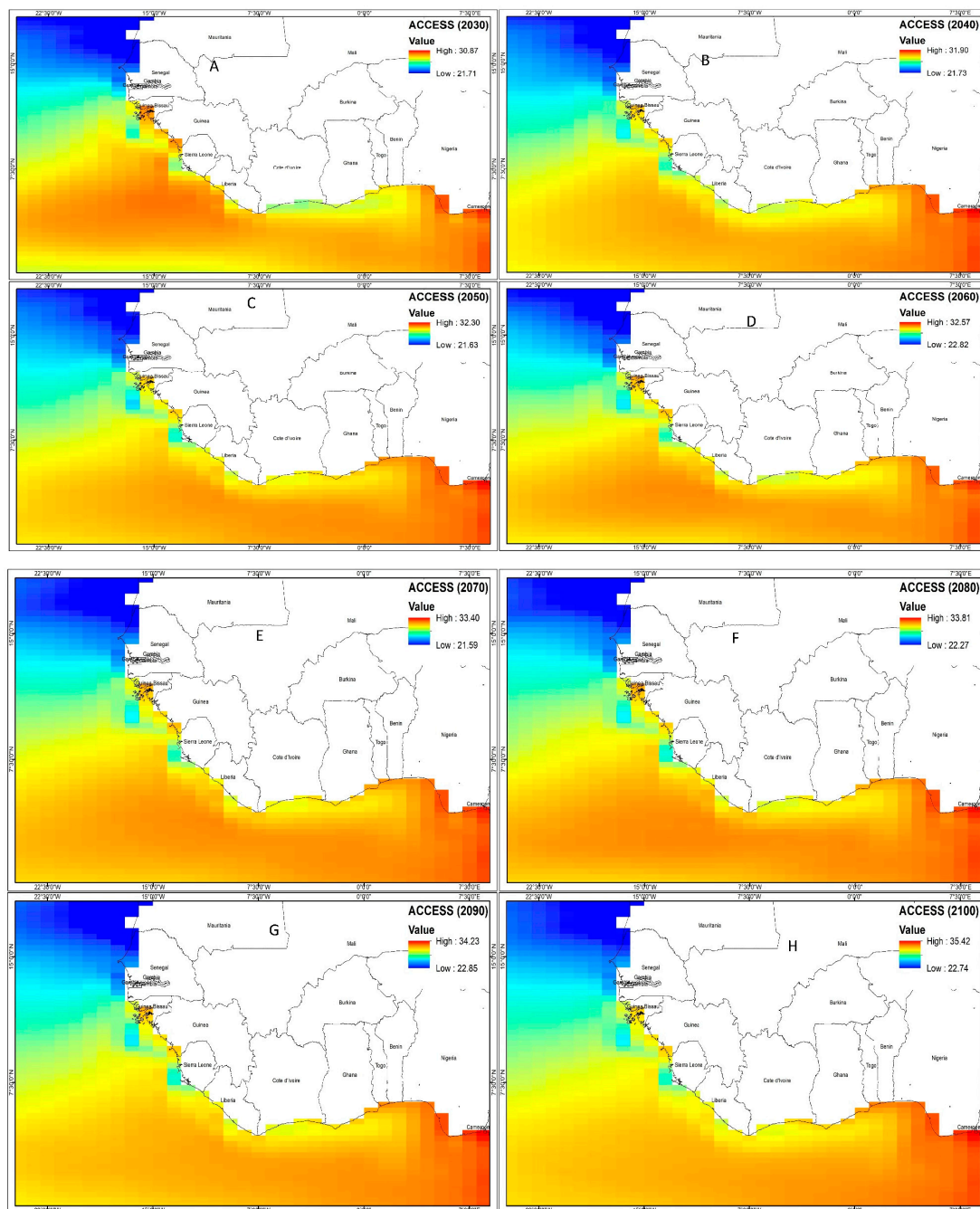

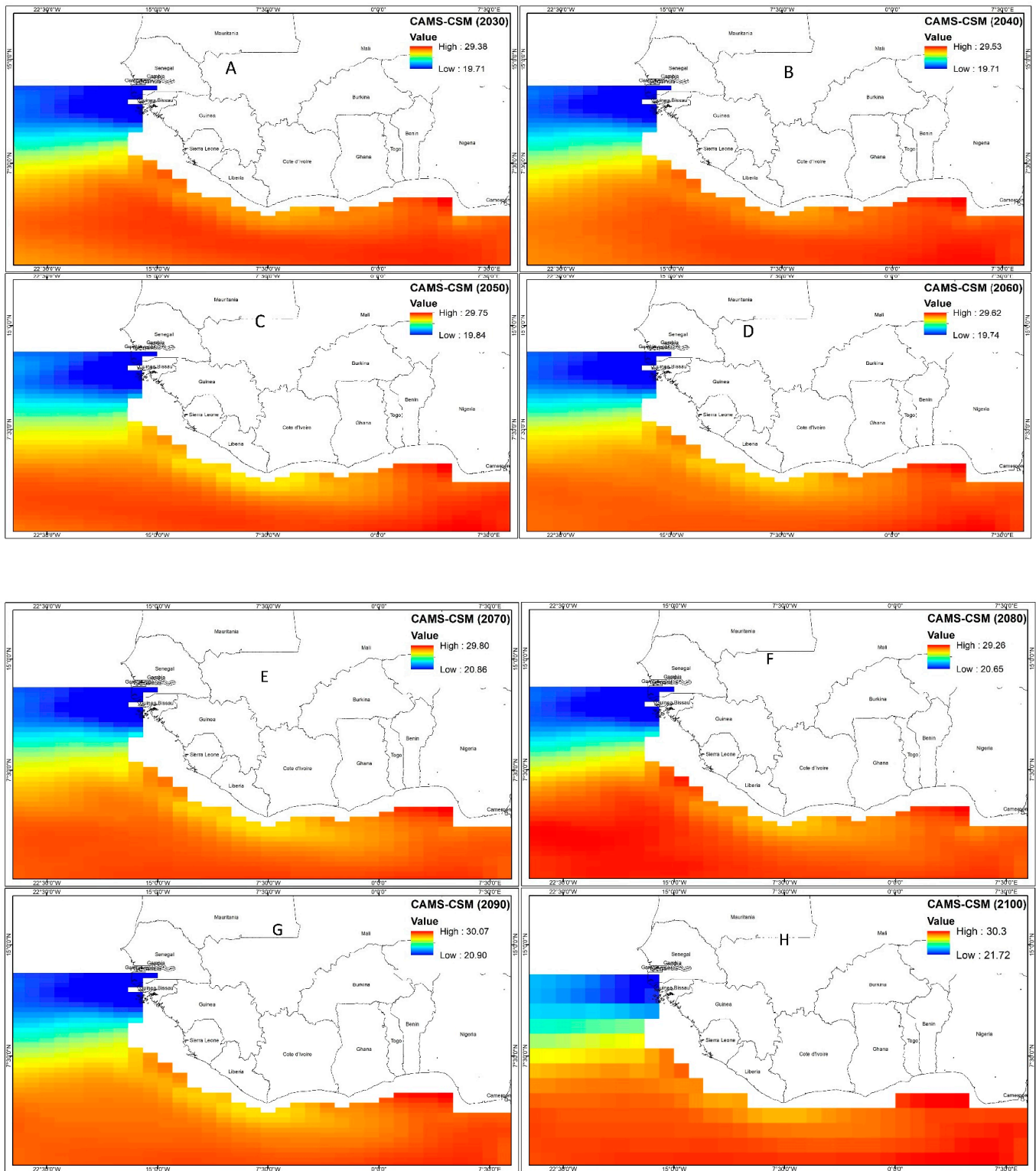**Figure 7.** CMIP6 ACCESS model's SST projection.

The projected warming is expected to continue unabated with the individual model showing 32.57 °C as the sea surface temperature for the Guinean coast and 22.82 °C for the Western Sahel in 2060, as shown in Figure 7D, while in 2070 (Figure 7E), the model projection indicates 32.40 °C and 21.58 °C for the high- and low-warming regions, respectively. In 2080 (Figure 7F), model projection captures the mean SST of the high-warming region as 33.81 °C and 22.27 °C for the low, and the upward warming swing is projected to remain in 2090 (Figure 7G) with 34.23 °C for the high- and 22.85 °C for the low-warming regions; the individual model projection in 2100 (Figure 7H) is expected to record the highest sea surface temperature, with 35.42 °C for the Guinean coast and 22.74 °C for the Western Sahel. The accelerated warming of and increased sea surface temperature projected by this model imply the intensification of increased extreme climate events given the role of ocean–atmosphere feedback and the ENSO mechanism [6].

The CAMS-CSM outputs shown in Figure 8A–H capture the future projection of mean sea surface temperature (SST) in 2030 for the high-warming region as 29.38 °C and 19.71 °C for the low-warming region of the GOG, with a further increase expected in 2040, as the high-warming region will record a temperature of 29.53 °C and a wet bias of 19.71 °C. Additional warming values of 29.75 °C and 19.84 °C will be recorded in 2050 for the high- and low-warming regions, while the SST variability in the 2060 projection will see the GOG experience 29.62 °C and 19.74 °C in the Western Sahel. The future SST projection for 2070 is expected to be significantly warmer than 2060 given the variability values of 29.82 °C and 20.86 °C for both the Guinean coast and the Western Sahel, as well as 29.26 °C for the Gulf of Guinea Coast and 20.85 °C for the Western Sahel in 2080. The year 2090 is projected to be warmer, with 30.07 °C and 20.90 °C for the high- and low-warming regions, respectively, with 2100 recording 30.3 °C for the high- and 21.72 °C for the low-warming regions of the study area, as demonstrated in Figure 8.

The model simulations of future SSTs by CAM-ESM in 2030, as shown in Figure 9A–H, are projected to be 30.82 °C and 20.08 °C for the Guinean coast and the Western Sahel, respectively, while in 2040, 31.56 °C and 21.16 °C are projected for the Gulf of Guinea coast and the Western Sahel. Increasing significant warming values are projected for the entire study domain in 2050 and 2060, with 31.78 °C and 21.05 °C for the high- and low-warming regions, while 32.41 °C and 20.80 °C are projected as the future sea surface temperatures in 2060 for the Guinea coast and the Western Sahel, respectively. In 2070, the warming pattern of the ocean is projected to continue with 32.94 °C and 21.57 °C for the high- and low-warming regions of the GOG with further warming projections of 34.17 °C and 21.58 °C, respectively. The year 2090 is projected to be significantly warmer, with 34.74 °C for the Guinean coast and 22.117 °C for the Western Sahel. The year 2100 is projected to experience a record ocean warming result, with mean sea surface temperatures of 35.45 °C and 22.30 °C for the Guinean coast and the Western Sahel, respectively.

The CMCC CMIP6 bias-corrected simulation of future SSTs for the GOG from 2030–20100, as shown in Figure 10A–H, projects SSTs in 2030 to be 29.64 °C and 18.80° for the high-warming and the Western Sahel regions. A further warming bias is projected in 2040, with 30.41 °C and 18.73 °C for the high- and low-warming regions. The model further projects the future SST in 2050 to be 30.87 °C, while the low-warming region is projected to be 20.23 °C. Additional warming biases are projected for 2060 to be 30.54 °C and 20.13 °C. The model projections for 2070 by CMCC-ESM were 31.78 °C and 21.23 for both the high- and low-warming regions, respectively. The projection for 2080 is expected to be considerably higher than for 2070, with 32.60 °C for the warning coastal region of the GOG and 21.69 °C for the Western Sahel. The future SST projection for 2090 is expected to be lower than 2080 for the GOG, with 32.15 °C for the high- and 21.65° for the low-warming regions. In 2100, significant warming and an increased SST variability are projected for the GOG, with 32.88 °C and 22.23 °C for the high- and low-warming regions, respectively.
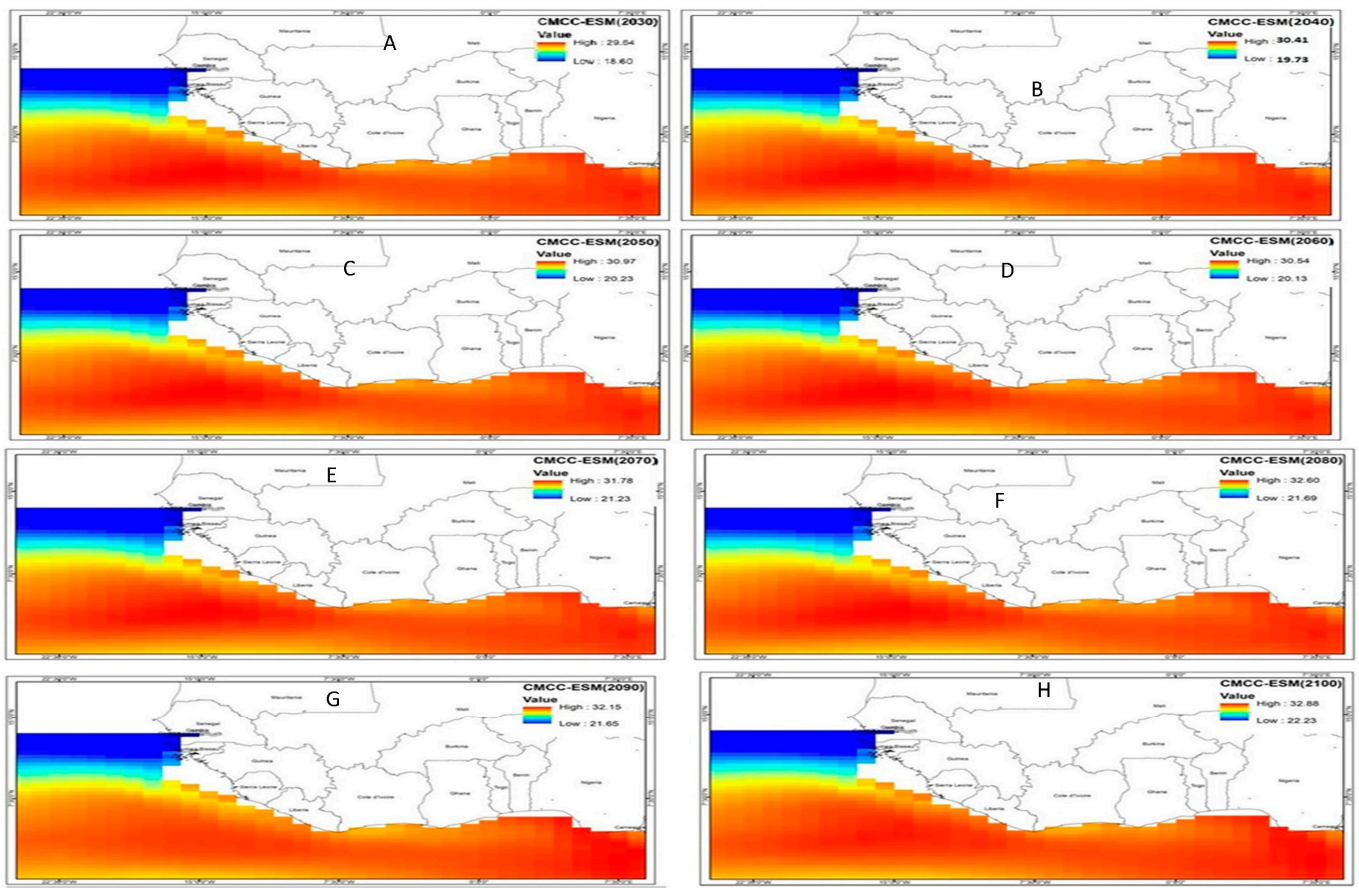
Figure 8. CMIP6 CAMS-CSM model's SST projection. (**A**) 2030, (**B**) 2040, (**C**) 2050, (**D**) 2060, (**E**) 2070, (**F**) 2080, (**G**) 2090, (**H**) 2100.
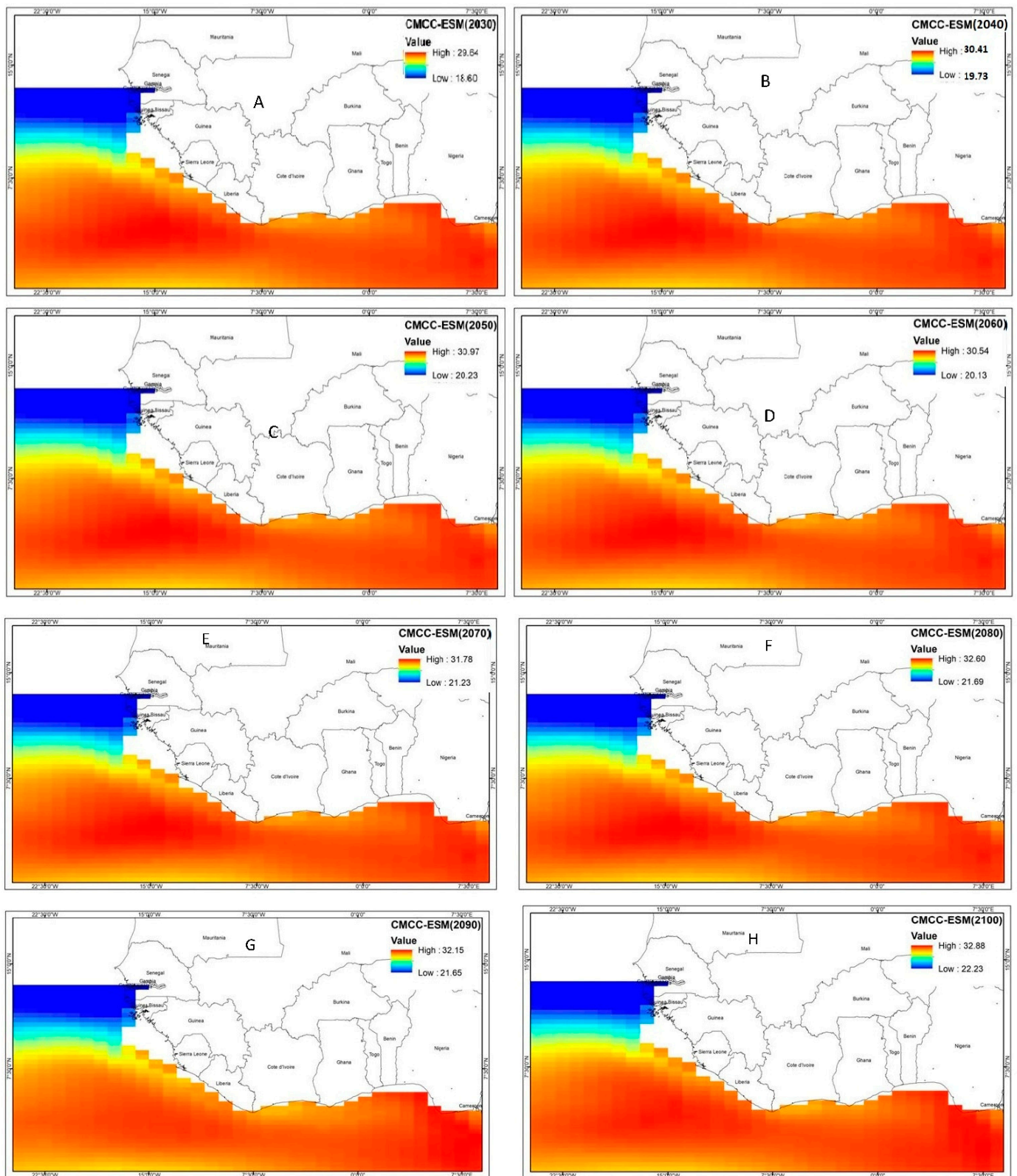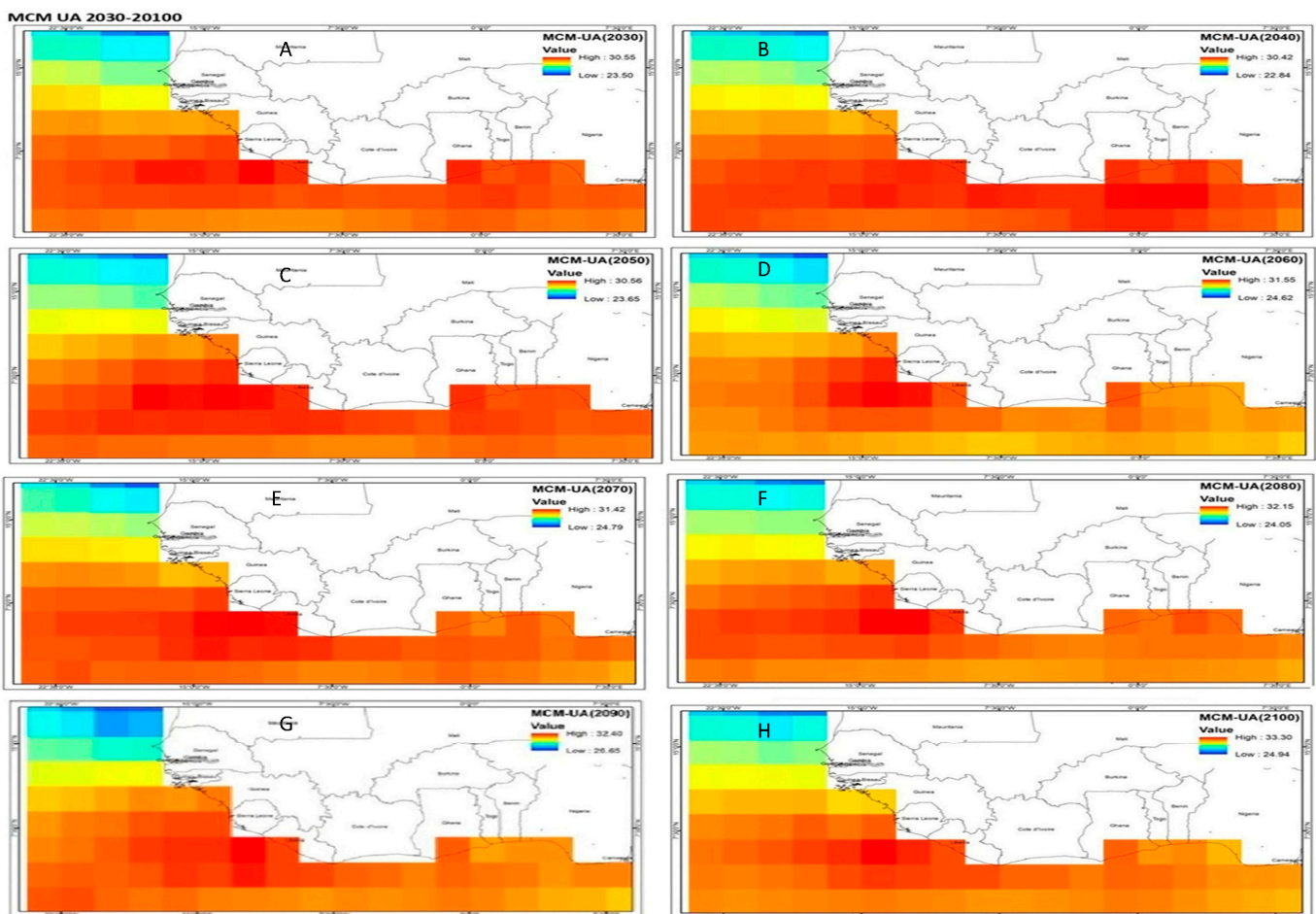
Figure 9. CMIP6-Can ESM model simulations of future SST projections. (Model outputs (**A**) 2030, (**B**) 2040, (**C**) 2050, (**D**) 2060, (**E**) 2070, (**F**) 2080, (**G**) 2090, (**H**) 2100).

Figure 10. CMIP6-CMCC model simulations of future SSTs.

Relatedly, the MCM-UA individual model shown in Figure 11A–H projects a warming bias of 30.55 °C as the mean sea surface temperature for the Guinean coast and 22.50 °C for the Western Sahel. In 2040, a cold bias is projected for the Guinean coast, at 30.42°, while a warm bias is expected over the Western Gulf of Guinea. The MCM model further captures the future SST projections for 2050 as 30.56 °C and 23.65 °C for the high- and low-warming regions, respectively. The year 2060 is projected to be significantly warmer than the preceding year (2050), with 31.55 °C for the Guinean coast and 24.62° for the Western Sahel. Similarly, reduced warming and a cold tongue are projected for the Guinea coast in 2070, at 3.42 °C, while the western flank of the GOG is projected to be slightly warmer at 24.79 °C. The 2070 projection is followed by sustained sea surface temperature warming projected to continue in 2080, with the Guinean coast recording 32.15 °C, while the Western Sahel is projected to be 24.05°. The model's SST future projections of the Gulf of Guinea in 2090 is 32.40 °C for the Guinean coast and 26.65 °C for the low-warming region of the study area, indicating that the Western Sahel will experience a significantly warmer climate in the future. An increased warming bias is further projected for 2100 as the Guinea coast is projected to warm up by 33.3 °C, and a cold bias is expected in the Western Sahel, with 24.90 °C as the sea surface temperature.

Figure 11. CMIP6 MCM model simulations of future SSTs. Model outputs with (**A**) 2030, (**B**) 2040, (**C**) 2050, (**D**) 2060, (**E**) 2070, (**F**) 2080, (**G**) 2090, (**H**) 2100.

4. Discussion

The spatial climatology of the historical data (1940–2014) and the CMIP6 simulations (2030–2100) were presented in the preceding section. It is important to underline that most of the models successfully reproduced the spatial patterns of SSTs over the GOG and the Western Sahel. However, the highest sea surface temperature (SST) value was produced by CAM-ESM (35.48 °C and 22.39 °C), indicating that the model overestimated the SST climatology, while the lowest values were for 2030 (29.38° and 19.71 °°C), implying the persistence of a warming bias in the Guinean cost and cold tongue along the Western Sahel. These results clearly show the influence of ENSO as the dominant driver of SST variability as evidenced by the warm bias and cold tongue in the Western flank of the Guinean coast. This suggests that all the models overestimated SST for the Guinean coast when juxtaposed with the observed dataset. The historical ERA5 data are used to validate the projected changes in the SST and, as shown in the results presented in the preceding section, the bias-corrected data are consistent with the observed data for the climatological mean period.

The findings from the CMIP6 model simulation further reveal that the SST is projected to increase by 1.03 °C between 2030 and 2040 in the Western GOG, with most of the warming projected to occur in 2090 and 2100. The projected warming bias demonstrated by the CMIP6 models was unsurprising as RCP 8.5 assumed higher GHG emissions leading to fossil fuel development [20]. Similarly, the SST for the Guinean coast known for its high warming was projected to increase by 4.61 °C between 2030 and 2100, with the SST expected to be substantially higher in the far than the near period in the study domain, although the projected warming was not homogenous as substantial increases in the multimodal mean SST were expected more often for the Guinea coast than the Western

Sahel. Similarly, [66], in their studies of bias-corrected CMIP 3 and CMIP 5, affirmed that coupled models exhibited sizable biases in the mean position of the West African Monsoon. Furthermore, the outcome of their analysis revealed that most models contained a warm bias in the Equatorial Atlantic and a southward shift of the ITCZ in coupled models; this southward bias was also examined in other studies conducted by [67,68]. Other studies that have been carried out using the GCM CMIP simulation include those of [69] who asserted that the Coupled Model Intercomparison Project Phase 5 (CMIP5) historical simulations underestimated SST seasonal cooling from April/May to August over the northern Gulf of Guinea, and suggested that this could have been driven by the incorrect seasonality of precipitation over the southern coastline of West Africa. Similar studies conducted by [70] on the projected sea surface temperature over the Equatorial Pacific posited that the warm pool region was projected to experience enhanced warming along the Equatorial Pacific. Overall, the future SST of the GOG is projected to become warmer in the future and the magnitude of change depends on future GHG scenarios. The projected warming presented in this study can impact marine ecosystems, fish, and the local climate.

4.1. Statistical Evaluation of the CMIP6 Models' Performance

This section examines the ability of the CMIP6 models to simulate the observed historical simulation. Several methods of validating the performance of the GCM-driven CMIP6 simulation exist in the literature, and they include the Nash–Sutcliffe efficiency (NSE), the Root Mean Square Error (RMSE) or the Root Mean Square Deviation (RMSD), the Mean Absolute Error (MAE), the Percentage Bias (PBIAS), and the Correlation Coefficient (Cr). These techniques have been employed by different researchers for the validation of the bias-corrected CMIP6 simulation [45,71–73]. However, in this study, the performance of the GCM-CMIP6 model in simulating the observed dataset was evaluated using the correlation coefficient. Consequently, the ability of each of the models used in the study to reproduce the spatial pattern of the SST over the GOG was evaluated/validated against the ERA5 reanalysis data in 1940–2014 using a statistical analysis.

A regression analysis is very useful when it comes to studying the relationship between variables. The regression analysis can identify the cause and effect of one variable regarding another variable. Variables are the main part of a regression analysis. There are dependent variables (or criterion variables) and independent variables (or predictor variables). In a multiple regression, the independent variables can also be added to the model to explain the cause and effect of dependent variables. Hence, dependent variables can be predicted by building better models using a multiple regression analysis.

An overview of the models used and their respective countries, spatial resolutions which is $10° \times 10°$ including the period of coverage for both the historical and the simulated are presented in Table 2. The table further highlights the emission scenarios and shared socio-economic pathways. The table is significant as it provide a background of the models used in the study.

Multiple Regression

Multiple regression models can be presented by the following equation:

$$Y = \beta_0 + \beta_{1\times1} + \beta_{2\times2} + \beta_{3\times3} + \beta_{4\times4} + \beta_{5\times5} + \beta_{6\times6} \ldots\ldots + \beta_n X_n + \varepsilon \tag{1}$$

where Y is the CanESM (dependent variable), X_1, X_2, X_3, X_4, and X_5 (independent variables) are ACCESS, CAMS-CSM, CMCC-ESM, EC-Earth3, MCM-UA, and MPI-ESM, respectively. β_1, β_2, β_3, β_4, and β_5 are the model coefficients of the six independent variables. β_0 is a constant, while ε is the error.

The outcome of the model regression analysis conducted, as shown in Table 2, Figures 12a–f and 13, indicates that all the models, namely, ACCESS, CAMS-CSM. CAN-ESM, CMCC, MCM-UA, and MPI-ESM have r values of 0.10 for ACCES, as shown in Figure 10A; 0.0185 for the CAMS-CSM model, shown in Figure 10B; and 0.0681 for CAN-ESM, shown in Figure 10C. Similarly, CMCC denoted in Figure 10D has R-values of 0.0919 and 0.107

for MCM-UA, as shown in Figure 10E, with 0.013 for MP-ESM in Figure 10F. The weakest correlation was the CAMS-CSM model, with an R-value of 0.01, while the strongest correlation was MCM-UA, with 0.13, given the fact that the closer the r-value moved to +1, the stronger the correction between the variables of interest, while −1 implied a negative correlation. The summary regression statistic further indicates that there is a positive correlation between the individual models and the ERA5 historical data in 1940–2014.

Table 2. Considered climate models and their grid resolutions as well as numbers of simulations during the historical and future periods, along with the future scenarios.

Climate Modeling Centers	CMIPs	Spatial Resolution	Number of Simulations			Future Scenarios
			Historical Period	Future Periods		
Can ESM	CanESM2	1.0° × 1.0°	1940–2022	2014–2100	8.5	RCPs 4.5 and 8.5
	CanESM5	1.0° × 1.0°	1940–2022	2014–2100	85	SSPs 2–4.5 and 5–8.5
CMCC-ESM	CMCC-ESM	1.0° × 1.0°	1940–2022	2014–2100	8.5	RCPs 4.5 and 8.5
	CMCC-ESM	1.0° × 1.0°	1940–2022	2014–2100	8.5	SSPs 2–4.5 and 5–8.5
ACCESS	ACCESS	1.0° × 1.0°	1940–2022	2014–2100	85	RCPs 4.5 and 8.5
	ACCESS	1.0° × 1.0°	1940–2022	2014–2100	8.5	SSPs 2–4.5 and 5–8.5
EC-Earth3	EC-Earth3	1.4° × 1.5°	1940–2022	2014–2100	8.5	RCPs 4.5 and 8.5
	EC-Earth3	1.4° × 1.4°	1940–2022	2014–2100	8.5	SSPs 2–4.5 and 5–8.5
MPI	MPI-ESM-LR	1.0° × 1.0°	1940–2022	2014–2100	8.5	RCPs 4.5 and 8.5
	MPI-ESM1-2-LR	1.0° × 1.0°	1940–2022	2014–2100	8.5	SSPs 2–4.5 and 5–8.5
MCM-UA	MCM-UA	2.0° × 2.0°	1940–2022	2014–2100	8.5	RCPs 4.5 and 8.5
	MCM-UA	2.0° × 2.0°	1940–2022	2014–2100	8.5	SSPs 2–4.5 and 5–8.5
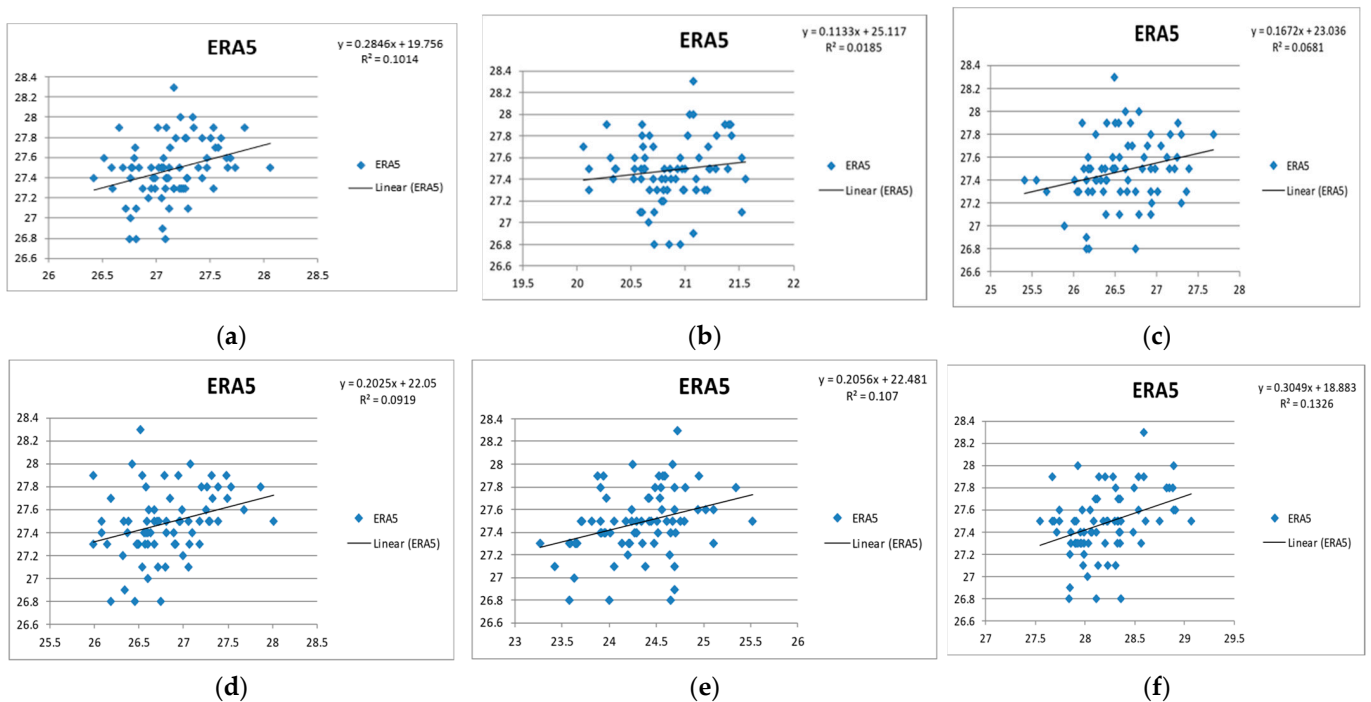
Figure 12. Evaluation of CMIP6 model's performance against ERA5 regression analysis: (**e**) Figure 10: Evaluation of CMIP6: (**a**) ACCESS, (**b**) CAMS-CSM, (**c**) CAN-ESM, (**d**) CMCC-MCM-UA, and (**f**) MPI-ESM models.
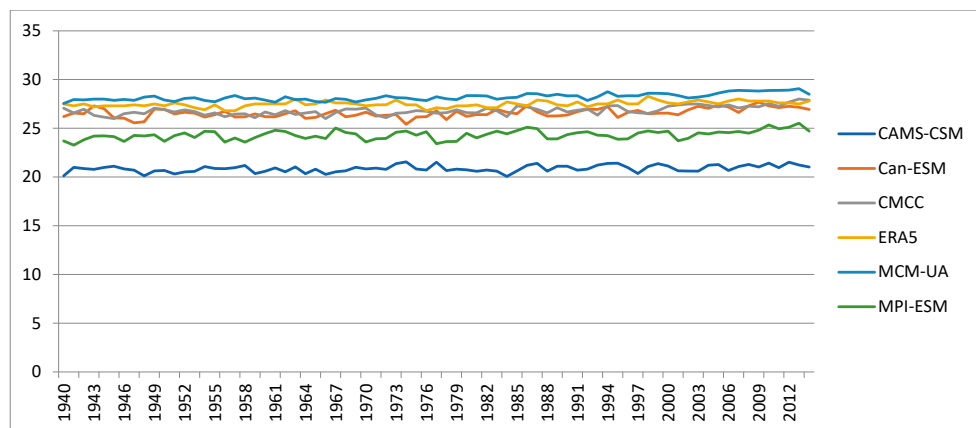
Figure 13. Summary output of CMIP6 models and ERA5 dataset.

The summary output of the performance of the CMIP6 models for the historical and the ERA5 observed sea surface temperature data is presented in Figure 13. A cursory look at Figure 13 demonstrates the fidelity and consistency of the selected models in reproducing the observed ERA5 data, except for CAMS-CSM.

4.2. Test of Significance

The Pearson product-moment correlation coefficient (r) carried out on the CMIP6 models to validate the performance of the models as shown in Table 3. The statistical analysis carried under SPSS s indicates that ACCESS, CAMS-CSM, CAN-ESM, CMCC, and MCM UA were statistically significant in the 1-tailed significance test with the r values of 0.00, 0.00, 0.00, 0.00, and 0.00 at 0.00 ($p < 0.05$), respectively as shown in Table 4. This implied that the individual models performed well and were therefore suitable for simulating the statistical patterns of SSTs over the Gulf of Guinea.

Table 3. Coefficient of correlations.

		ERA5	ACCESS	CAMS	CanESM	CMCC	MCM
	ERA5	1.000	0.318	0.136	0.261	0.303	0.364
	ACCESS	0.318	1.000	0.378	0.318	0.522	0.497
Pearson Correlation	CAMS	0.136	0.378	1.000	0.230	0.274	0.466
	CanESM	0.261	0.318	0.230	1.000	0.463	0.525
	CMCC	0.303	0.522	0.274	0.463	1.000	0.559
	MCM	0.364	0.497	0.466	0.525	0.559	1.000
	MPI	0.327	0.177	0.241	0.349	0.399	0.460
	ERA5		0.003	0.122	0.012	0.004	0.001
	ACCESS	0.003		0.000	0.003	0.000	0.000
Sig. (1-tailed)	CAMS	0.122	0.000		0.024	0.009	0.000
	CanESM	0.012	0.003	0.024		0.000	0.000
	CMCC	0.004	0.000	0.009	0.000		0.000
	MCM	0.001	0.000	0.000	0.000	0.000	
	MPI	0.002	0.065	0.018	0.001	0.000	0.000
	ERA5	75	75	75	75	75	75
	ACCESS	75	75	75	75	75	75
N	CAMS	75	75	75	75	75	75
	CanESM	75	75	75	75	75	75
	CMCC	75	75	75	75	75	75
	MCM	75	75	75	75	75	75
	MPI	75	75	75	75	75	75

Table 4. ANOVA [a].

Model		Sum of Squares	df	Mean Square	F	Sig.
1	Regression	0.837	1	0.837	11.161	0.001 [b]
	Residual	5.477	73	0.075		
	Total	6.314	74			

[a] Dependent variable: ERA5. [b] Predictors: (constant), MCM.

The outcome of the model regression analysis conducted, as shown in Table 3, including the ANOVA in Table 4 and the descriptives shown in the study indicates that the F value of 11.61 is statistically significant at ($p < 0.05$). This implies that there is a statistically significant difference between the means of the different model outputs. The coefficients of the models and their significance is presented in Table 5 which further lends credence to the suitability of the different models used in the study.

Table 5. Coefficients.

Model		Unstandardized Coefficients		Standardized Coefficients	t	Sig.
		B	Std. Error	Beta		
1	(Constant)	18.883	2.574		7.336	0.000
	MCM	0.305	0.091	0.364	3.341	0.001

The histogram graph in Figure 14 shows that the CMIP6 model outputs are normal distributions for future trends (2030–2100). The histogram graph was created as one of the assumptions that should be checked before building a forecasting model to ascertain model normality and linearity. It was important to evaluate the goodness of fit and the statistical significance of the estimated SST model outputs of the constructed regression models; the techniques commonly used to verify the goodness-of-fit values of regression models are hypothesis testing, R-squared, and the analysis of the residuals. In this case, the histogram was skewed towards positive correlations suggesting that the CMIP6 model simulation and the observed results were likely to lead to a skill teleconnection between the SST anomalies and West African rainfall climatology.
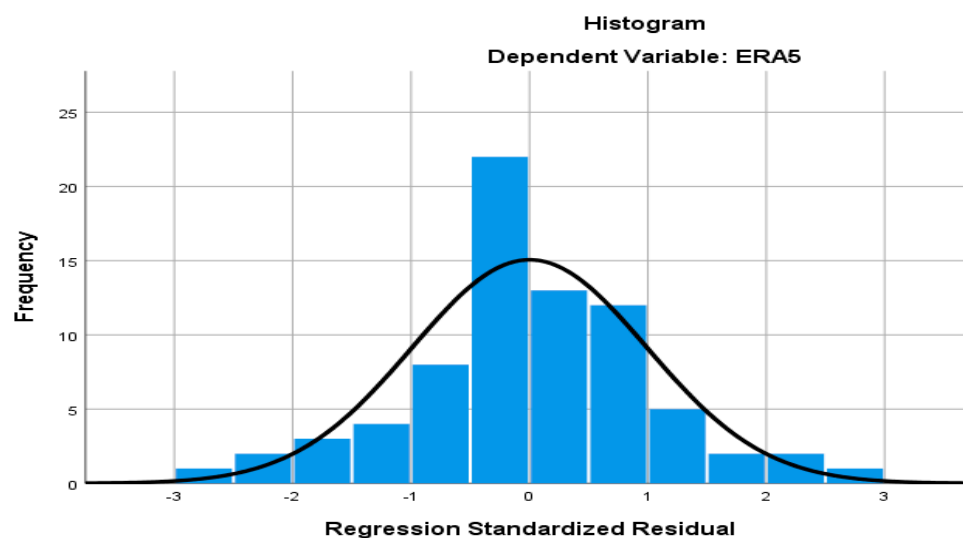

Figure 14. Histogram of the CMIP6 outputs.

The output from the CMIP6 model for all the models showed a smooth trend for the future scenarios (2015–2100). The scatter plot in Figure 15 shows the normal probability plot between the ERA5 observational data and the CMIP6 future SST simulation. The residual plot further shows that the relationship between the ERA5 observational data and the CMIP6 simulation is linear. Therefore, the probability plots indicate that the error terms are indeed normally distributed. In statistics, the P-P plot compares the observed cumulative Distribution Function (CDF) of the standardized residual to the expected CDF of the normal distribution. The normal probability plot indicates whether the residuals follow a normal distribution, in which case, the points follow a straight line, as is evident in Figure 14.
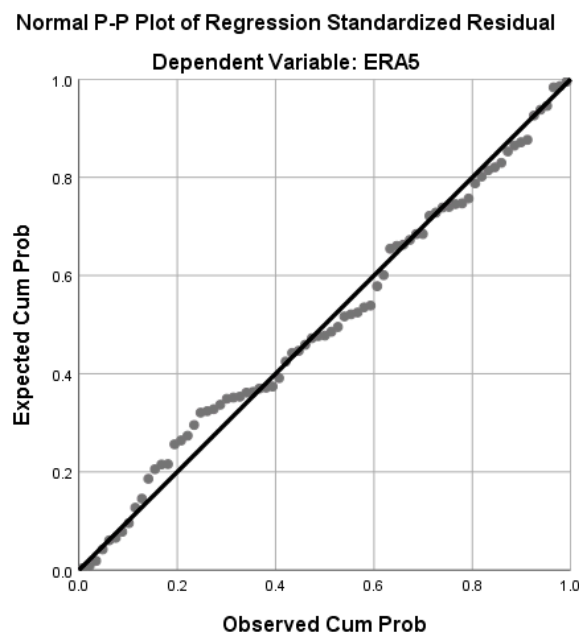

Figure 15. Plot of the observed ERA5 against CMIP6 model outputs.

The results, however, show that the CMIP6 multi-model ensemble mean values (and CVs) for the six indices have similar magnitudes and patterns of variations as the reanalysis data for the Gulf of Guinea, except the MCM-UA model (USA) (Table 6).

Table 6. Collinearity diagnostics.

Collinearity Diagnostics							
Model	Dimension	Eigenvalue	Condition Index	Variance Proportions			
				(Constant)	ACCESS	MCMUA	MPIESM
1	1	1.999	1.000	0.00	0.00		
	2	0.001	43.820	1.00	1.00		
2	1	2.999	1.000	0.00	0.00	0.00	
	2	0.001	52.817	0.30	0.07	0.00	
	3	5.885×10^{-5}	225.739	0.70	0.93	1.00	
3	1	3.999	1.000	0.00	0.00	0.00	0.00
	2	0.001	60.981	0.22	0.06	0.00	0.00
	3	0.000	175.706	0.31	0.13	0.04	0.99
	4	5.869×10^{-5}	261.029	0.46	0.81	0.96	0.01
4	1	4.999	1.000	0.00	0.00	0.00	0.00
	2	0.001	66.901	0.20	0.04	0.00	0.00
	3	0.000	188.768	0.19	0.02	0.01	0.95
	4	6.915×10^{-5}	268.854	0.06	0.14	0.33	0.05
	5	5.783×10^{-5}	294.013	0.54	0.81	0.66	0.00

5. Summary and Conclusions

The study evaluated the performances of bias-corrected GCM-CMIP6 models in stimulating the historical and future projections of SSTs over the Gulf of Guinea involving ACCESS-CM2 (Australia), CAMS-CSM1-0 (China), CanESM5-CanOE (Canada), CMCC-ESM2 (Italy), HadGEM3-GC31-LL (UK), EC-Earth3-CC (Europe), MCM-UA-1-0 (USA), and MPI-ESM1-2-LR (Germany), while ERA5 reanalysis data were used as the observed/historical data for the validation of the models. Given the fact that GCM spatial resolutions are often too coarse, the bias-corrected dataset was developed using Empirical Quantile Mapping (EQM) for the historical (1940–2014) and projected (2015–2100) periods to achieve reliable projections at the regional and local scales. The CMIP6 GCM model projection further revealed that ACCESS-CM2 CAMS-CSM1-0, CanESM5, CMCC-ESM2, and MCM-UA performed better in reproducing the observed SST climatology. The future SST projections by the models indicate that, on average, SSTs will warm up by 1.03 °C between 2030 and 2040, and a projection of 35 °C by 100 against the historical observation of 30 °C was simulated by the models between 1970 and 2014 for the high-warming region and 21° for the Western Sahel. The model evaluation using the coefficient of regression indicated that all the models, namely, ACCESS, CAMS-CSM, CAN-ESM, CMCC, MUM, and MP-ESM, had R values of 0.10, 0.01, 0.06, 0.09, 0.10, and 0.013, respectively. The weakest correlation was for the CAMS-CSM model, at 0.01, while the strongest correlation was for MCM-UA, at 0.13, which further demonstrated the fidelity of the models in reproducing the observed SST climatology of the Guinean coast.

In view of the foregoing, the study concludes that the eight CMIP6 models that were examined both underestimate and overestimate SSTs over the GOG relative to the ERA5 reanalysis dataset, which is evident over the GOG. The cold bias was mainly focused on over the Western Sahel, which was the most obvious during the cold season, while the warm bias dominated in the Guinean coast. The models were generally successful in representing the spatial variabilities of the climatological mean sea surface temperatures. One of the implications of projected, future SST warming is that it will drive changes in the meridional and zonal SST gradients with a deleterious impact on the local climate and beyond and the location of the Intertropical Convergence Zone (ITCZ), which is a function of the underlying SST and the Equatorial Meridional SST gradients. In addition, small spatial differences in SST warming can also trigger changes in the winds and, hence, rainfall strength and distribution in the future. Finally, the study concludes that the projected increase in future SSTs over the GOG will be higher in the far period end than the near-term climate. Overall, the bias-corrected CMIP6 projections can be used for multiple assessments related to climate and hydrological impact studies and for developing mitigation measures under a warming climate.

The authors are grateful to the two anonymous reviewers for their time and effort in reviewing this work. These suggestions have made this work much better.

References

1. Watson, R.T.; Core Writing Team (Eds.) *IPCC: Climate Change 2001: Synthesis Report—A Contribution of Working Groups I, II, and III to the Third Assessment Report of the Intergovernmental Panel on Climate Change*; Cambridge University Press: Cambridge, UK; New York, NY, USA, 2001; p. 398.
2. Wijffels, S.; Roemmich, D.; Monselesan, D.; Church, J.; Gilson, J. Ocean Temperatures Chronicle the Ongoing Warming of Earth. *Nat. Clim. Change* **2016**, *6*, 337–342. [CrossRef]
3. Sung, H.M.; Kim, J.; Lee, J.H.; Shim, S.; Boo, K.O.; Ha, J.C.; Kim, Y.H. Future Changes in the Global and Regional Sea Level Rise and Sea Surface Temperature Based on CMIP6 Models. *Atmosphere* **2021**, *2*, 90. [CrossRef]
4. Roberts, C.D.; Palmer, M.D.; Mcneall, D.; Collins, M. Quantifying the Likelihood of a Continued Hiatus in Global Warming. *Nat. Clim. Change* **2001**, *5*, 337. [CrossRef]
5. Dado, J.M.B.; Takahashi, H.G. Potentail impact of sea surface temperature on rainfall over the western Philippines. *Prog. Earth Planet. Sci.* **2017**, *4*, 1–12. [CrossRef]
6. Lübbecke, J.F.; Belen-Fonseca, B.R.; Richter, I.; Martín-Rey, M.; Losada, T.; Polo, I.; Keenlyside, N.S. Equatorial Atlantic Variability Modes, Mechanisms, and Global Teleconnections. *Wiley Interdiscip. Rev. Clim. Change* **2018**, *9*, e527. [CrossRef]
7. Rowell, D.P. Stimulating SST Teleconnections to Africa: What is the state of the Art? *J. Clim.* **2013**, *26*, 5397–5418. [CrossRef]
8. Palmer, P.I.; Wainwright, C.M.; Dong, B.; Maidment, R.I.; Wheeler, K.G.; Gedney, N.; Hickman, J.E.; Madani, N.; Folwell, S.S.; Abdo, G.; et al. Drivers and Impacts of Eastern African Rainfall Variability. *Nat. Rev. Earth Environ.* **2023**, *4*, 254–270. [CrossRef]
9. Newell, R.E.; Kidson, J.E. African mean wind changes between Sahelian wet and dry periods. *J. Climatol.* **1984**, *4*, 27. [CrossRef]
10. Bah, H. Towards the prediction of Sahelian rainfall from sea surface temperatures in the Gulf of Guinea. *Tellus* **1987**, *39A*, 39–48. [CrossRef]
11. Adeniye, M.O. Modeling the Impact of Changes in Atlantic Sea Surface Temperature on the Climate of West Africa. *J. Meteorol. Atmos. Phys.* **2017**, *129*, 187–210. [CrossRef]
12. World Bank. *The Next Generation Africa Climate Business Plan*; World Bank: Washington, DC, USA, 2020.
13. UNFCCC. *The State of the Climate: Extreme Events and Major Impacts*; UNFCCC: Bonn, Germany, 2021.
14. Seager, R.; Naik, N.; Vogel, L. Does global warming cause intensified interannual hydroclimate Variability? *J. Clim.* **2012**, *25*, 3355–3372. [CrossRef]
15. IPCC. Climate Change 2007: The Physical Science Basis. Contribution of Working Group I to the Fourth Assessment Report of the Intergovernmental Panel on Climate Change. Cambridge University Press: Cambridge, UK; New York, NY, USA, 2007.
16. IPCC. Climate Change 2013: The Physical Science Basis. Contribution of Working Group I to the Fifth Assessment Report of the Intergovernmental Panel on Climate Change. Stocker, T.F., Qin, D., Plattner, G.-K., Tignor, M., Allen, S.K., Boschung, J., Nauels, A., Xia, Y., Bex, V., Midgley, P.M., Eds.; Cambridge University Press: Cambridge, UK; New York, NY, USA, 2013; p. 1535.
17. Burls, N.J.; Reason, C.J.C.; Penven, P.; Philander, S.G. Energetics of the Tropical Atlantic zonal mode. *J. Clim.* **2012**, *25*, 7442–7466. [CrossRef]
18. Breugem, W.P.; Hazeleger, W.; Haarsma, R.J. Multimodal Study of Tropical Atlantic Variability and Change. *Geophys. Res. Lett.* **2006**, *33*, L23706. [CrossRef]
19. Ahmed, K.; Shahid, S.; Sachindra, D.A.; Nawaz, N.; Chung, E.S. Fidelity Assessment of General Circulation Model Simulated Precipitation and Temperature over Pakistan using a Feature Selection Method. *J. Hydrol.* **2019**, *573*, 281–298. [CrossRef]
20. Jose, P.M.; Dwarakish, G.S. Bias Correction and Trend Analysis of Temperature Data by a High-Resolution CMIP6 Model over a Tropical River Basin. *Asia-Pac. J. Atmos. Sci.* **2022**, *58*, 97–115. [CrossRef]
21. Sonali, P.; Kumar, D.N. Review of recent advances in climate change detection and attribution studies: A large-scale hydro climatological perspective. *J. Water Clim. Change* **2020**, *11*, 1–29. [CrossRef]
22. Chokkavarapu, N.; Mandla, V.R. Comparative Study of GCMs, RCMs, Downscaling and Hydrological Models: A review toward future climate change impact estimation. *SN Appl. Sci.* **2019**, *1*, 1698. [CrossRef]
23. Ayugi, B.; Zhihong, J.; Zhu, H.; Ngoma, H.; Babaousmail, H.; Rizwan, K.; Dike, V. Comparison of CMIP6 and CMIP5 models in simulating mean and extreme precipitation over East Africa. *Int. J. Climatol.* **2021**, *41*, 6474–6496. [CrossRef]
24. Liz, Z.; Liu, T.; Huang, Y.; Peng, J.; Ling, Y. Evaluation of the CMIP6 Precipitation Simulations over Global Land. *Earth's Future* **2022**, *10*, 1–21.
25. Holthuijzen, M.; Beckage, B.; Clemins, P.J.; Higdon, D.; Winter, J.M. Robust bias correction of precipitation extremes using a novel hybrid empirical quantile-mapping method. *Theor. Appl. Climatol.* **2022**, *149*, 863–882. [CrossRef]
26. Ekström, M.; Grose, M.R.; Whetton, P.H. An appraisal of downscaling methods used in climate change research. *Clim. Change* **2015**, *6*, 301–319. [CrossRef]
27. Lafon, T.; Dadson, S.; Buys, G.; Prudhomme, C. Bias correction of daily precipitation simulated by a regional climate model: A comparison of methods. *Int. J. Climatol.* **2013**, *33*, 1367–1381. [CrossRef]
28. Leander, R.; Buishand, T. A Resampling of regional climate model output for the simulation of extreme river flows. *J. Hydrol.* **2007**, *332*, 487–496. [CrossRef]
29. Pierce, D.W.; Cayan, D.R.; Maurer, E.P.; Abatzoglou, J.T.; Hegewisch, K.C. Improved bias correction techniques for hydrological simulations of climate change. *J. Hydrometeorol.* **2015**, *16*, 2421–2442. [CrossRef]
30. Shrestha, M.; Acharya, S.C.; Shrestha, P.K. Bias correction of climate models for hydrological modeling–are simple methods still useful? *Meteorol. Appl.* **2017**, *24*, 531–539. [CrossRef]

31. Hoffmann, H.; Rath, T. Meteorologically consistent bias correction of climate time series for agricultural models. *Theor. Appl. Climatol.* **2012**, *110*, 129–141. [CrossRef]

32. Zia, A.; Bomblies, A.; Schroth, A.W.; Koliba, C.; Isles, P.D.; Tsai, Y.; Mohammed, I.N.; Bucini, G.; Clemins, P.J.; Turnbull, S.; et al. Coupled impacts of climate and land use change across a river–lake continuum: Insights from an integrated assessment model of lake Champlain's Missisquoi basin, 2000–2040. *Environ. Res. Lett.* **2016**, *11*, 114026. [CrossRef]

33. Trasher, B.; Maurer, E.P.; McKellar, C.; Dufy, P.B. Technical Note: Bias correcting climate model simulated daily temperature extremes with quantile mapping. *Hydrol. Earth Syst. Sci.* **2012**, *16*, 3309–3314. [CrossRef]

34. Maraun, D. Bias correction, quantile mapping, and downscaling: Revisiting the inflation issue. *J. Clim.* **2010**, *26*, 2137–2143. [CrossRef]

35. Giorgi, F.; Gutowski, W.J. Regional Dynamical Downscaling and the CORDEX Initiative. *Annu. Rev. Environ. Resour.* **2015**, *40*, 467–490. [CrossRef]

36. Mearns, L.; Giorgi, F.; Whetton, P.; Pabon, D.; Hulme, M.; Lal, M. *Guidelines for Use of Climate Scenarios Developed from Regional Climate Model Experiments*; Data Distribution Centre of the Intergovernmental Panel on Climate Change: Geneva, Switzerland, 2003; pp. 1–38.

37. Feser, F.; Rockel, B.; von Storch, H.; Winterfeldt, J.; Zahn, M. Regional climate models add value to global model data: A review and selected examples. *Bull. Am. Meteorol. Soc.* **2011**, *92*, 1181–1192. [CrossRef]

38. Caldwell, P.; Chin, H.N.S.; Bader, D.C.; Bala, G. Evaluation of a WRF dynamical downscaling simulation over California. *Clim. Change* **2009**, *95*, 499–521. [CrossRef]

39. Leung, L.R.; Mearns, L.O.; Giorgi, F.; Wilby, R.L. Regional climate research: Needs and opportunities. *Bull. Am. Meteorol. Soc.* **2003**, *84*, 89–95.

40. Mearns, L.O.; Sain, S.; Leung, L.R.; Bukovsky, M.S.; McGinnis, S.; Biner, S.; Caya, D.; Arritt, R.W.; Gutowski, W.; Takle, E.; et al. Climate change projections of the North American Regional Climate Change Assessment Program (NARCCAP). *Clim. Change* **2013**, *120*, 965–975. [CrossRef]

41. Hanssen-Bauer, I.; Achberger, C.; Benestad, R.; Chen, D.; Førland, E. Statistical downscaling of climate scenarios over Scandinavia. *Clim. Res.* **2005**, *29*, 255–268. [CrossRef]

42. Gudmundsson, L.; Bremnes, J.B.; Haugen, J.E.; Engen-Skaugen, T. Technical Note: Downscaling RCM precipitation to the station scale using statistical transformations—A comparison of methods. *Hydrol. Earth Syst. Sci.* **2012**, *16*, 3383–3390. [CrossRef]

43. Mudbhatkal, A.; Mahesha, A. Bias correction methods for hydrologic impact studies over India's Western Ghat basins. *J. Hydrol. Eng.* **2018**, *23*, 05017030. [CrossRef]

44. Smitha, P.S.; Narasimhan, B.; Sudheer, K.P.; Annamalai, H. An improved bias correction method of daily rainfall data using a sliding window technique for climate change impact assessment. *J. Hydrol.* **2018**, *556*, 100–118. [CrossRef]

45. Mendez, M.; Maathuis, B.; Hein-Griggs, D.; Alvarado-Gamboa, L.F. Performance evaluation of bias correction methods for climate change monthly precipitation projections over Costa Rica. *Water* **2020**, *12*, 482. [CrossRef]

46. White, R.H.; Toumi, R. The limitations of bias correcting regional climate model inputs. *Geophys. Res. Lett.* **2013**, *40*, 2907–2912. [CrossRef]

47. Lanzante, J.R.; Dixon, K.W.; Adams-Smith, D.; Nath, M.J.; Whitlock, C.E. Evaluation of some distributional downscaling methods as applied to daily precipitation with an eye towards extremes. *Int. J. Climatol.* **2021**, *41*, 3186–3202. [CrossRef]

48. Christensen, J.H.; Boberg, F.; Christensen, O.B.; Lucas-Picher, P. On the Need for Bias Correction of Regional Climate Change Projections of Temperature and Precipitation. *J. Geophys. Res. Lett.* **2008**, *35*, L20709. [CrossRef]

49. Byun, K.; Hamlet, A.F. An improved empirical quantile mapping procedure for bias-correction of climate change projections. In Proceedings of the An American Geophysical Union, Fall Meeting, San Francisco, CA, USA, 9–13 December 2019.

50. Heo, J.; Ahn, H.; Shin, J.; Kjeldsen, T.; Jeong, C. Probability Distributions for a Quantile Mapping Technique for a Bias Correction of Precipitation Data: A Case Study to Precipitation Data Under Climate Change. *Water* **2019**, *11*, 1475. [CrossRef]

51. Déqué, M. Frequency of precipitation and temperature extremes over France in an anthropogenic scenario: Model results and statistical correction according to observed values. *Glob. Planet Change* **2007**, *57*, 16–26. [CrossRef]

52. Shabalova, M.V.; van Deursen, W.P.; Buishand, T.A. Assessing future discharge of the river Rhine using regional climate model integrations and a hydrological model. *Clim. Res.* **2003**, *23*, 233–246. [CrossRef]

53. Teutschbein, C.; Seibert, J. Bias correction of regional climate model simulations for hydrological climate-change impact studies: Review and evaluation of different methods. *J. Hydrol.* **2012**, *456*, 12–29. [CrossRef]

54. Ezéchiel, O.; Eric, A.A.; Josué, Z.E.; Eliézer, B.I.; Amédée, C. Comparative study of seven bias correction methods applied to three Regional Climate Models in Mekrou catchment (Benin, West Africa). *Int. J. Curr. Eng. Technol.* **2016**, *6*, 1831–1840.

55. Amengual, A.; Homar, V.; Romero, R.; Alonso, S.; Ramis, C. A statistical adjustment of regional climate: Application to Platja de Palma. *Spain J. Clim.* **2012**, *25*, 939–957. [CrossRef]

56. Gutjahr, O.; Heinemann, G. Comparing precipitation bias correction methods for high-resolution regional climate simulations using COSMO-CLM: Effects on extreme values and climate change signal. *Theor. Appl. Climatol.* **2013**, *114*, 511–529. [CrossRef]

57. Volosciuk, C.; Maraun, D.; Vrac, M.; Widmann, M. A combined statistical bias correction and stochastic downscaling method for precipitation. *Hydrol. Earth Syst. Sci.* **2017**, *21*, 1693–1719. [CrossRef]

58. Li, H.; Sheffield, J.; Wood, E.F. Bias correction of monthly precipitation and temperature fields from intergovernmental panel on climate change AR4 models using equidistant quantile matching. *J. Geophys. Res. Atmos.* **2010**, *115*, 1–20. [CrossRef]

59. Cannon, A.J.; Sobie, S.R.; Murdock, T.Q. Bias correction of GCM precipitation by quantile mapping: How well do methods preserve changes in quantiles and extremes? *J. Clim.* **2015**, *28*, 6938–6959. [CrossRef]

60. Sahoo, S.; Dey, S.; Dhar, A.; Debsakar, A.; Predham, B. On projected hydrological scenarios under the influence of bias-corrected climatic variables and LULC. *Ecol. Indic.* **2019**, *106*, 105440. [CrossRef]

61. Eyring, V.; Bony, S.; Meehl, G.A.; Senior, C.A.; Stevens, B.; Stouffer, R.J.; Taylor, K.E. Overview of the Coupled Model Intercomparison Project Phase 6 (CMIP6) experimental design and organization. *Geosci. Model Dev.* **2016**, *9*, 1937–1958. [CrossRef]

62. Gidden, M.J.; Riahi, K.; Smith, S.J.; Fujimori, S.; Luderer, G.; Kriegler, E.; Van Vuuren, D.P.; Van Den Berg, M.; Feng, L.; Klein, D.; et al. Global emissions pathways under different socioeconomic scenarios for use in CMIP6: A dataset of harmonized emissions trajectories through the end of the century. *Geosci. Model Dev.* **2019**, *12*, 1443–1475. [CrossRef]

63. Odekunle, T.O.; Eludoyin, A.O. Sea surface temperature pattern and its implication on rainfall variability over the Gulf of Guinea. *Int. J. Climatol.* **2008**, *28*, 1507–1517. [CrossRef]

64. Ojo, O. *The Climates of West Africa*; Heinemann: London, UK, 1977; p. 219.

65. Iloeje, N.P. *A New Geography of Nigeria*; Longman: London, UK, 1981; p. 259.

66. Raper, S.C.B.; Cubasch, U. Emulation of the Results from a Coupled General Circulation Model using a Simple Climate Model. *Geophys. Res. Lett.* **1996**, *23*, 1107–1110. [CrossRef]

67. Siongco, A.C.; Hohenegger, C.; Stevens, B. The Atlantic ITCZ bias in CMIP5 models. *Clim. Dyn.* **2015**, *45*, 5–6. [CrossRef]

68. Steinig, S.; Harlaß, J.; Park, W.; Latif, M. Sahel rainfall strength and onset improvements due to more realistic Atlantic cold tongue development in a climate model. *Sci. Rep.* **2018**, *8*, 2569. [CrossRef] [PubMed]

69. Dunning, C.M.; Allan, R.P.; Black, E. Identification of deficiencies in seasonal rainfall simulated by CMIP5 climate models. *Environ. Res. Lett.* **2017**, *12*, 1748–9326. [CrossRef]

70. Brown, J.N.; Langlais, C.; Gupta, A.S. Projected Sea Surface Temperature Changes in the Equatorial Pacific Relative to the Warm Pool Edge. *Elsevier J. Sea Res.* **2015**, *11*, 47–58. [CrossRef]

71. Bhatt, B.C.; Sobolowski, S.; Higuchi, A. Simulation of Diurnal Rainfall variability over the maritime continent with high-resolution regional climate model. *J. Jpn. Meteorol. Soc. Jpn.* **2016**, *94A*, 89–103. [CrossRef]

72. Cai, T.T.; Guo, Z.; Ma, R. Statistical Inference for High-Dimensional Generalized Linear Models with Binary Outcomes. *J. Am. Statitsical Assoc.* **2021**, *118*, 1319–1332. [CrossRef] [PubMed]

73. Rhymee, H.; Shams, S.; Ratnayake, U.; Rahman, E.K.A. Comparing Statistical Downscaling and Arithmetic Mean in Simulating CMIP6 Multi-Model Ensemble over Brunei. *Hydrology* **2022**, *9*, 161. [CrossRef]